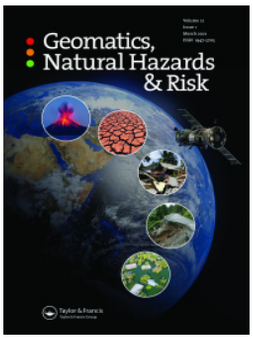

Geomatics, Natural Hazards and Risk

ISSN: 1947-5705 (Print) 1947-5713 (Online) Journal homepage: www.tandfonline.com/journals/tgnh20

Anomalies of land-atmospheric parameters in the 2023 Turkey earthquake (Mw7.8) using GNSS and ERA5

Li Li , Huafeng Ma , Galina Dick , Jens Wickert , Enchen Wu , Mingsong Zhang , Zehua Meng & Yuqing Huang

To cite this article: Li Li , Huafeng Ma , Galina Dick , Jens Wickert , Enchen Wu , Mingsong Zhang , Zehua Meng & Yuqing Huang (2026) Anomalies of land-atmospheric parameters in the 2023 Turkey earthquake (Mw7.8) using GNSS and ERA5, Geomatics, Natural Hazards and Risk, 17:1, 2637789, DOI: 10.1080/19475705.2026.2637789

To link to this article: https://doi.org/10.1080/19475705.2026.2637789

© 2026 The Author(s). Published by Informa UK Limited, trading as Taylor & Francis Group.

Published online: 27 Feb 2026.

Submit your article to this journal

Article views: 258

View related articles

View Crossmark data

Full Terms & Conditions of access and use can be found at
https://www.tandfonline.com/action/journalInformation?journalCode=tgnh20

GEOMATICS, NATURAL HAZARDS AND RISK
2026, VOL. 17, NO. 1, 2637789
https://doi.org/10.1080/19475705.2026.2637789

Taylor & Francis
Taylor & Francis Group

RESEARCH ARTICLE

OPEN ACCESS Check for updates

Anomalies of land-atmospheric parameters in the 2023 Turkey earthquake (Mw7.8) using GNSS and ERA5

Li Li[a,b], Huafeng Ma[a,c], Galina Dick[b], Jens Wickert[b], Enchen Wu[d], Mingsong Zhang[a], Zehua Meng[a] and Yuqing Huang[a]

[a]Research Center of BeiDou Navigation and Environmental Remote Sensing, Suzhou University of Science and Technology, Suzhou, China; [b]Section 1.1: Space Geodetic Techniques, GFZ Helmholtz Centre for Geosciences, Potsdam, Germany; [c]School of Geosciences and Info-Physics, Central South University, Changsha, China; [d]National Synchrotron Radiation Laboratory, University of Science and Technology of China, Hefei, China

ABSTRACT

The Turkey earthquake (Mw 7.8) caused severe damage to Turkey and Syria on Feb. 6, 2023. It was observed that anomalies of land surface and atmospheric multi-parameters were associated with the land–atmosphere–ionosphere coupling (LAIC) mechanism. The data from the Global Navigation Satellite System (GNSS) and the fifth-generation ECMWF reanalysis (ERA5) were employed to establish two GNSS precipitable water vapour (PWV) interpolation models using Random Forest (RF) and extreme gradient boosting (XGBoost) algorithms. Anomalous variations of land-atmospheric parameters were analyzed using Sliding Interquartile Range (SIQR) and Z-score (ZS) methods. The results show that the root mean square errors (RMSEs) of the RF-PWV and XGBoost-PWV are 1.15 and 1.32 mm, respectively. On Feb. 5, the maximum ZS values of the surface latent heat flux (SLHF) and total column water vapour (TCWV) reached 20.03 and 4.71, respectively. On Feb. 6, the ZS of air temperature (AT) and surface pressure (SP) reached extremes of 4.18 and −7.87, respectively. The PWV decreased rapidly 1 h before the earthquake and recovered quickly to its peak thereafter. Small anomalies (≤1.61 TECU) in total electron content (TEC) were detected on Feb. 4–5. However, substantial increases in the number and magnitude of the TEC anomalies were observed on Feb. 6, with a maximum of 14.83 TECU.

ARTICLE HISTORY
Received 8 August 2025
Accepted 20 February 2026

KEYWORDS
Land-atmospheric parameters; anomaly; Turkey; earthquake; GNSS; ERA5

1. Introduction

Earthquakes are natural hazards caused by brittle fractures under tectonic stress in the lithosphere. The mechanism of earthquake occurrence is influenced by both crustal movements and physical environmental factors. Strong earthquakes cause severe spatial destruction, triggering secondary disasters such as rainfall and debris flows and hindering post-disaster rescue operations (Kato and Ben-Zion 2021; Wirth et al. 2022). Therefore, earthquake forecasting has significant practical value. It is classified into long-, medium-, and short-term forecasting based on a time scale. Short-term earthquake forecasting offers the greatest practical value, but faces substantial challenges (Rundle et al. 2021).

The energy release of Earth's interior before and after an earthquake could disturb the atmospheric environment, causing anomalies of land-atmospheric multi-parameters. These anomalies, which typically occur months or days prior to the earthquake, could be considered seismic precursors (Pulinets and Ouzounov 2011). Post-earthquake anomalies may be associated with residual energy in the earthquake region or may reflect the dynamic recovery of the land-atmospheric system (Mansouri Daneshvar et al. 2015).

Fujiwara et al. (2004) reported that the enhanced horizontal polarisation of radio waves commonly occurred within five days prior to earthquakes ($Mw \geq 4.8$) in the Japanese region. The anomalies of horizontal polarisation originate from the troposphere or the lower atmosphere. Numerous studies have found that the surface temperature (ST) (Bhardwaj et al. 2017; Khan et al. 2025), surface latent heat flux

CONTACT Li Li gszl.lili@gmail.com; Huafeng Ma 2213021037@post.usts.edu.cn

© 2026 The Author(s). Published by Informa UK Limited, trading as Taylor & Francis Group.
This is an Open Access article distributed under the terms of the Creative Commons Attribution-NonCommercial License (http://creativecommons.org/licenses/by-nc/4.0/), which permits unrestricted non-commercial use, distribution, and reproduction in any medium, provided the original work is properly cited. The terms on which this article has been published allow the posting of the Accepted Manuscript in a repository by the author(s) or with their consent.

(SLHF) (Zhang et al. 2013; Yang et al. 2023), air temperature (AT) (Draz et al. 2023; Nath et al. 2024), outgoing longwave radiation (OLR) (Kong et al. 2018; Shah et al. 2024), and surface pressure (SP) (Jing et al. 2013; Hamama and Yamamoto 2021) exhibit anomalies before and after earthquakes. The anomalies of multiple land-atmospheric multi-parameters are primarily linked to fault creep and frictional heating before the earthquake, greenhouse gas emissions, and post-earthquake energy release (Bhardwaj et al. 2017).

The precipitable water vapour (PWV) is defined as the total atmospheric water vapour contained in a unit vertical column. The PWV directly reflects the moisture content in the air and shows significant anomalous variations in the troposphere during earthquakes (Dey et al. 2004; Guo et al. 2023). The total electron content (TEC) represents the total number of free electrons within a unit vertical column. The TEC is commonly expressed as the integral of the electron density along the global navigation satellite system (GNSS) signal path. It reflects ionospheric activity levels and may exhibit earthquake-induced anomalies (Simha et al. 2023; Haider et al. 2024). Moreover, extensive research has demonstrated obvious mutual anomalies among the land surface, tropospheric, and ionospheric regions, which indicate a land–atmosphere–ionosphere coupling (LAIC) mechanism (Jing Feng et al. 2019; Xie et al. 2025).

On Feb. 6, 2023, the northward compression of the Arabian Plate against the Eurasian Plate resulted in the westward motion of the Anatolian microplate along the East Anatolian Fault (EAF), characterised by left-lateral strike-slip movement. The sudden release of long-term accumulated stress triggered two strong earthquakes in Turkey, both of which were over Mw 7.0. The mainshock (Mw 7.8) occurred at 01:17 UTC. Its epicentre was located at 37.226°N and 37.014°E, with a focal depth of approximately 10 km. The hypocenter was situated on the EAF, which exhibited a left-lateral strike-slip rupture (Luhrmann et al. 2025). The aftershock (Mw 7.5) occurred at 10:24 UTC, with a focal depth of 7.4 km. Its epicentre was located at 36.893°N, 37.189°E, on the Surgu Fault, approximately 100 km from the mainshock (Mw 7.8) (Jing et al. 2024). The earthquakes caused severe destruction in the regions of Turkey and Syria, resulting in approximately 50,000 fatalities and more than 100,000 injuries. A total of 19,284 buildings collapsed, and 373,038 buildings experienced varying degrees of damage (Mavroulis et al. 2023). Heavy rainfall occurred in southern Turkey after the earthquake, significantly impeding rescue operations (Ozkula et al. 2023). Therefore, anomalous land-atmospheric multi-parameters are highly important for earthquake prediction and secondary disaster prevention.

Although previous studies have explored anomalous variations in land–atmosphere parameters before and after earthquakes using GNSS, ERA5, or other datasets, they have generally focused on a limited range of parameters using simple methods. Moreover, the missing GNSS-PWV data caused by ground rupture, power outages, and other factors due to earthquake events have not been effectively addressed. Therefore, the interpolation of missing GNSS-PWV time series provides reliable support for analysing water vapour anomalies associated with seismic activity. Secondly, the anomalous variations of surface, tropospheric, and ionospheric multi-parameters will be systematically analysed using the Z-score (ZS) and sliding interquartile range (SIQR) methods.

The remainders are organised as follows: Section 2 presents the data and methodologies used in the study. Section 3 describes the evaluation of the accuracy of the ERA5 total column water vapour (TCWV) method using GNSS-PWV and develops two GNSS-PWV interpolation models based on the random forest (RF) and extreme gradient boosting (XGBoost) algorithms to fill the missing GNSS-PWV before and after an earthquake. Section 4 analyses the displacements of GNSS stations on the day of the earthquake and the anomalies of land-atmosphere multi-parameters (ST, AT, SP, SLHF, OLR, TCWV, PWV and TEC) before and after the earthquake using the ZS and SIQR methods. Section 5 presents a Discussion and Conclusions.

2. Data and methods

2.1. Data

2.1.1. GNSS

Turkey is located at the convergence of the Eurasian, Arabian, and African tectonic plates and encompasses two of the world's most active continental faults: the EAF and the North Anatolian Fault (NAF). Its unique geography has resulted in frequent seismic activities. On Feb. 6, 2023, two strong earthquakes occurred on the

EAF, with magnitudes of Mw 7.8 and Mw 7.5, followed by thousands of aftershocks, causing severe damage across 11 provinces (Kahramanmaras, Gaziantep, Sanliurfa, Diyarbakir, Adana, Adiyaman, Osmaniye, Hatay, Kilis, Malatya, and Elazig) in Turkey and three provinces (Idlib, Aleppo, and Raqqa) in Syria (Hussain et al. 2023; Kalaycı and Özkurt Çokgüngör 2023). The study region focuses on the 14 most affected provinces of Turkey and Syria, including surrounding areas, covering 34°N–40°N and 34°E–43°E. Fifteen GNSS stations were selected near the epicentre, and their distributions are shown in Figure 1.

The GNSS zenith tropospheric delay (ZTD) and GNSS-PWV were derived from two GNSS organisations, the Turkish National Permanent GNSS Network-Active (TUSAGA-Aktif) and the Nevada Geodetic Laboratory (NGL). The 1-second GNSS observation data were obtained from the TUSAGA-Aktif, which is part of the Turkish geospatial positioning service. However, it only provides GNSS data for the three days before and ten days after the earthquake because its website is designed primarily for monitoring seismic deformation. GNSS observations were processed using Pride PPP-AR GNSS software to obtain their three-dimensional displacements and GNSS-ZTD values at 15 stations (Geng et al. 2019). The hourly GNSS-PWV was obtained from GNSS-ZTD combined with ERA5-derived meteorological parameters (He et al. 2020).

Since 1996, the NGL has collected thousands of GNSS data from continuously operating reference stations (CORS) worldwide. The NGL processed the GNSS data using GIPSY to generate the GNSS-ZTD and its gradients, the GNSS-PWV, and the atmospheric weighted mean temperature (T_m). In this study, 300-s interval GNSS ZTD and PWV data from 15 GNSS stations during 2022–2024 were selected and resampled to 1-hour interval. They were used for the construction of the PWV interpolation model.

2.1.2. ERA5

ERA5 reanalysis data, provided by the European Centre for Medium-Range Weather Forecasts (ECMWF), offers both single-level and 37 pressure-level datasets, with a spatial resolution of $0.25° \times 0.25°$ and a temporal resolution of 1 h. In this study, 37 pressure-level data were used to obtain surface temperature (T_s), surface pressure (P_s), and T_m after horizontal interpolation and elevation correction at 15 GNSS

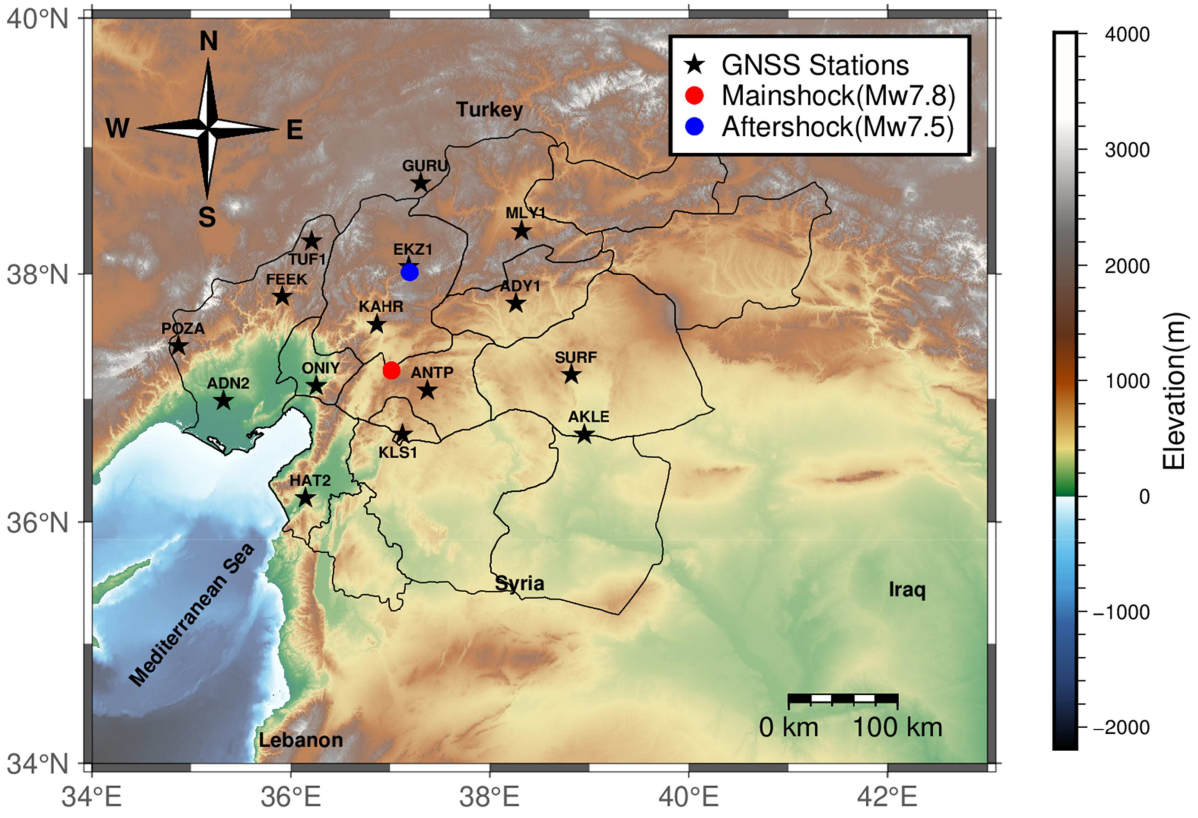

Figure 1. The distribution of 2 epicentres (Mw7.8 and Mw7.5) and 15 GNSS stations in the study region.

stations (Wang et al. 2025). The TCWV, ST, AT, SLHF, SP, total precipitation (*TP*), 10-m U-component of wind (U10), 10-m V-component of wind (V10), and OLR were obtained from a single-level ERA5 dataset. These variables were interpolated to 15 GNSS stations using inverse distance weighting.

The water vapour is primarily (approximately 99.5%) in the troposphere (Kaufman et al. 1997). TCWV and PWV can be used to quantify the water vapour content from the surface to the top of the troposphere. Therefore, both terms can be used interchangeably to represent atmospheric water vapour.

2.1.3. Geomagnetic and solar activity indices

The geomagnetic indices include the disturbance storm time index (Dst), the three-hourly geomagnetic index (Kp*10), and the linear scale of the Kp index (Ap), while the solar activity indices include the solar radio flux at a wavelength of 10.7 cm (F10.7). These data were obtained from the OMNIWeb database provided by the Goddard Space Flight Centre (GSFC) of the National Aeronautics and Space Administration (NASA). The OMNIWeb database integrates observations from multi-system satellites and releases consistent, high-quality near-Earth space environment activity indices after temporal normalisation. Generally, when Dst, Kp*10, Ap, and F10.7 satisfy the following conditions: $-50 \le \mathrm{Dst} < -30$, $0 \le \mathrm{Kp}*10 \le 40$, $0 \le \mathrm{Ap} \le 20$, and $0 \le \mathrm{F10.7} \le 140$, the levels of geomagnetic and solar activities are considered weak, indicating that these activities introduce minimal disturbance to the ionospheric TEC, as shown in Table 2.

2.1.4. TEC

The TEC data are derived from the 1-hour Global Ionosphere Map (GIM) products produced by the Polytechnic University of Catalonia (UPC, Spain) and distributed by the International GNSS Service (IGS). These products are distributed in the common data format (CDF) and are downloaded from NASA's Coordinated Data Analysis Web (CDAWeb). The GIM maps have a temporal resolution of 1 h and a spatial resolution of 5° longitude × 2.5° latitude with global coverage. This method is suitable for the accurate detection of ionospheric anomalies (Chen et al. 2019).

2.2. Methods

2.2.1. GNSS-PWV

The GNSS-PWV calculation requires GNSS-ZTD, ERA5-P_s, and ERA5-T_m in this study. ERA5-P_s is introduced into the Saastamoinen model (Equation 1) to calculate the zenith hydrostatic delay (ZHD). The difference between GNSS-ZTD and ZHD yields the zenith wet delay (ZWD). The conversion factor (λ)

Table 1. The locations of 15 GNSS stations and their distances to the epicentres (km).

GNSS	Lon (°E)	Lat (°N)	Height (m)	Distance to epicentre (Mw7.8)	Distance to epicentre (Mw7.5)
ANTP	37.374	37.065	886.883	36.56	106.35
KAHR	36.861	37.593	734.375	43.01	54.96
KLS1	37.124	36.713	660.785	57.91	144.52
ONIY	36.254	37.102	127.192	68.75	130.80
EKZ1	37.187	38.058	1328.87	93.78	5.30
FEEK	35.912	37.815	600.295	117.18	114.70
ADY1	38.261	37.761	741.176	125.06	97.54
TUF1	36.208	38.261	1504.764	135.09	90.72
HAT2	36.145	36.196	137.360	138.27	222.3
ADN2	35.323	36.983	69.302	152.34	200.87
SURF	38.818	37.192	680.765	159.81	169.45
GURU	37.308	38.717	1357.439	167.82	79.15
MLY1	38.319	38.342	1039.177	168.94	104.80
AKLE	38.948	36.710	385.281	181.16	211.91
POZA	34.872	37.422	826.401	190.68	214.67

Table 2. The activity levels of geomagnetic and solar activity indices.

Activity level	Dst (nT)	Kp*10	Ap (nT)	F10.7 (sfu)
Weak	[−50, −30)	[0, 40]	[0, 20]	[0, 140]
Moderate	[−100, −50)	(40, 50]	(20, 40]	(140, 200]
Strong	[−250, −100)	(50, 90]	(40, 60]	(200, 250]

was obtained using ERA5-T_m (Equation (2)). Then, the GNSS-PWV is subsequently derived from the product of the ZWD and λ (He et al. 2020; Li et al. 2022; 2025):

$$ZHD = \frac{0.0022768 \times P_S}{1 - 0.00266cos2\sigma - 0.00000028 \times h_s} \tag{1}$$

$$\lambda = \frac{10^3}{R_v \times \left(\frac{k_3}{T_m} + k_2'\right)} \tag{2}$$

$$GNSS - PWV = (GNSS - ZTD - ZHD) \times \lambda = ZWD \times \lambda \tag{3}$$

where P_S represents the surface pressure at the GNSS station (hPa), h_s represents the station height (m), λ represents the conversion factor, and σ represents the latitude of the stations (radians), R_v = 461.495 $(J{\cdot}kg^{-1}K^{-1})$, and k_2' = 16.48 $(K{\cdot}hpa^{-1})$, k_3 = 375463 $(K^2{\cdot}hpa^{-1})$.

2.2.2. Machine learning

(1) Random forest

RF is an ensemble learning algorithm based on the bootstrap bagging strategy that uses decision trees as weak learners. It is well known for its simple structure, robustness, and high training efficiency. RF handles high-dimensional feature data effectively without requiring feature selection and shows strong fault-tolerant ability to an imbalanced datasets. The core principle of RF is random sampling from the original dataset to create different training sub-datasets, which produce individual decision trees. Each decision tree generates its own prediction. The final regression output of the entire forest was obtained by averaging the predictions for all decision trees (Breiman 2001). The expression is as follows:

$$\hat{y} = \frac{1}{N}\sum_{i=1}^{N} f_i(X) \tag{4}$$

where N is the number of decision trees, f_i is the i-th decision tree, $\hat{y}$ is the output of the model, and X is the input feature.

(2) XGBoost

XGBoost is an ensemble-learning algorithm based on a gradient-boosted decision tree. It integrates multiple weak learners into one strong learner through a weighted combination. The method is known for its fast training speed and high prediction accuracy. The core principle of XGBoost is to sequentially build a series of decision trees. The process fits the residuals of the previous predictions by iteratively generating new trees. After data training, each tree falls into a specific leaf node that has a corresponding weight. The final prediction was obtained by summing the weighted outputs of all decision trees (Chen and Guestrin 2016):

$$\hat{y}_i^{(N)} = \sum_{n=1}^{N} f_n(x_i) = \hat{y}_i^{(N-1)} + f_N(x_i), f_n \in F \tag{5}$$

where N is the number of regression trees, $\hat{y}_i^{(N)}$ is the prediction of the sample (i) after the N-th iteration, $\hat{y}_i^{(N-1)}$ is the prediction of the previous N-1 trees, f_n is the model of the n-th tree, x_i is the input feature, $f_N(x_i)$ is the model of the N-th tree, and F is the function space of the regression tree.

2.2.3. Anomaly detection

(1) Sliding Interquartile Range

The SIQR is a statistical time-series anomaly detection method. A median-centred SIQR was employed in this study to improve the robustness of the anomaly detection. Compared with traditional SIQR,

median-centred SIQR is better suited for non-stationary time series with seasonal variation trends. This enhances the accuracy and robustness of the anomaly detection. A sliding window width should be set first, the data of each window will be arranged in chronological order, and then the 25th percentile is computed and labelled as Q1, representing the data below 25%. The median, labelled Q2, was the 50th percentile. The 75th percentile is labelled Q3. An anomaly threshold range centred on the median Q2 (Feng et al. 2023; Chen et al. 2024). The lower and upper bounds were calculated as follows:

$$Lower\ Bound = Q_2 - k \times (Q_3 - Q_1) \tag{6}$$

$$Upper\ Bound = Q_2 + k \times (Q_3 - Q_1) \tag{7}$$

where $k = 1.5$ is a sensitivity adjustment factor.

(2) Z-score

In this study, Z-score anomalies are calculated on a grid-wise basis using ERA5 data. The difference between the observation in an earthquake occurring year and the average of historical observations during the same period is treated as the signal, whereas the standard deviation of the historical observation during the same period serves as the noise. Dividing the signal by noise yields the ZS index, as shown in Equation 8. The magnitude of the ZS reflects not only how far the observation in the earthquake occurring year deviates from the average of historical observations during the same period but also how significant the deviation is relative to the background noise over historical observation during the same period (Jiao et al. 2023).

$$ZS(x, y, t) = \frac{v(x, y, t) - \overline{\mu(x, y)}}{\delta(x, y)} \tag{8}$$

where $ZS(x, y, t)$ refers to the ZS index, $v(x, y, t)$ represents the observation in the year of the earthquake, $\overline{\mu(x, y)}$ and $\delta(x, y)$ represents the mean and standard deviation of the historical observations during the same period.

In order to reduce the influence of climatic and geographical factors, a moving average was first applied to historical observations during the same period before calculating the mean and standard deviation. The selection criteria for the historical observations was that no earthquakes (Mw ≥ 5) occurred within the study region during the same period of other years, and at least 5-year historical data were selected, except for the year in which the earthquake occurred. To avoid the effects of solar radiation and human activities, data recorded between 00:00 and 03:00 at local time were selected (Choudhury et al. 2006).

The ZS method is generally assumed to have an approximate Gaussian distribution, where 68.3%, 95.4%, and 99.7% of the data fall within one, two, and three standard deviations, respectively. When ZS exceeds two standard deviations, it corresponds to a 95.4% confidence interval and is considered an anomaly. Therefore, the anomalous threshold for the ZS index was set to 2 in this study (Ambrosino et al. 2019; Jiao and Shan 2024).

2.2.4. Accuracy evaluation

The correlation coefficient (R), root-mean-square error (RMSE), and bias were used to evaluate the model's accuracy in this study. The specific formulae are as follows:

$$R = \frac{\sum_{i=1}^{n} (x_{model,i} - \overline{x_{model}}) \times (x_{true,i} - \overline{x_{true}})}{\sqrt{\sum_{i=1}^{n} (x_{model,i} - \overline{x_{model}})^2} \times \sqrt{\sum_{i=1}^{n} (x_{true,i} - \overline{x_{true}})^2}} \tag{9}$$

$$RMSE = \sqrt{\frac{\sum_{i=1}^{n} (x_{model,i} - x_{true,i})^2}{N}} \tag{10}$$

$$Bias = \frac{\sum_{i=1}^{N} (x_{model,i} - x_{true,i})}{N} \tag{11}$$

where $x_{model,i}$ is the i-th model output, $\overline{x_{model}}$ is the mean of all model outputs, $x_{true,i}$ is the i-th theoretical truth, $\overline{x_{true}}$ is the mean of all theoretical truths, and N is the number of samples. R is closer to 1, and the RMSE and bias are closer to zero, indicating better model accuracy.

3. GNSS-PWV interpolation model

The raw GNSS observation records are often interrupted because of problems with the GNSS receivers resulting from land surface ruptures or extreme weather during earthquakes. However, the ERA5-TCWV remained a relatively complete time series. Therefore, GNSS-PWV can be regarded as a reference for calibrating high-accuracy ERA5-TCWV. The calibrated ERA5-TCWV can be used to interpolate missing GNSS-PWV data.

3.1. Accuracy of ERA5-TCWV

Figure 2 shows comparisons between the ERA5-TCWV and GNSS-PWV at 15 GNSS stations during 2022–2024. As shown in Figure 2, the highest accuracy of the ERA5-TCWV was observed at EKZ1, with an RMSE of 1.47 mm, whereas the lowest accuracy of the ERA5-TCWV was found at FEEK, with an RMSE of 4.80 mm. The R values of the ERA5-TCWV and GNSS-PWV range from 0.92 to 0.96, with a mean of 0.95. Their biases range from −3.94 to 2.57 mm, with a mean of −0.12 mm, while their RMSEs range from 1.47 to 4.80 mm, with a mean of 2.33 mm, indicating a systematic discrepancy.

3.2. Model construction

The systematic discrepancies between the ERA5-TCWV and GNSS-PWV are shown in Figure 2. The data from 15 GNSS stations during 2022–2024 were utilised to construct regional PWV calibration models based on the RF and XGBoost algorithms. However, the data from the study period (Jan. 27–Feb. 11, 2023) were excluded to avoid any unintended overlap with the target event.

As shown in Figure 3, GNSS-PWV exhibits correlations with various meteorological variables (ST, AT, SP, TP, U10, and V10), with the day of year (DOY) and the hour of day (HOD). Previous studies have also shown pronounced annual and semi-annual PWV periodicities (Maghrabi 2019). Therefore, ERA5-

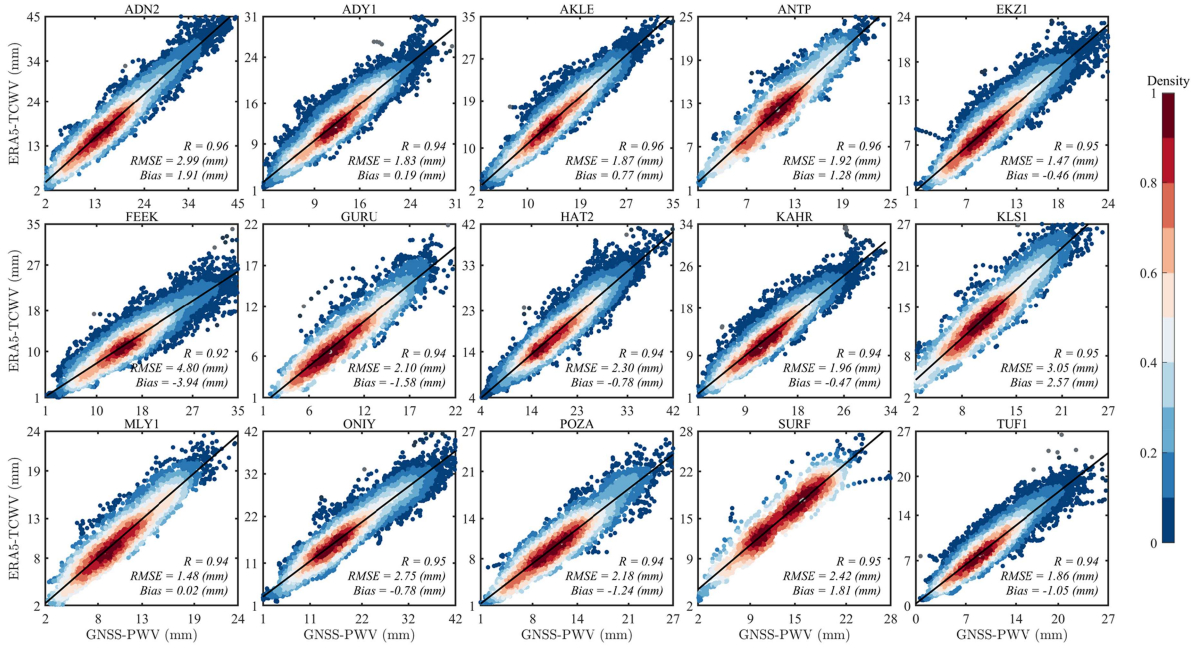

Figure 2. The comparisons of ERA5-TCWV and GNSS-PWV at 15 GNSS stations during 2022–2024.

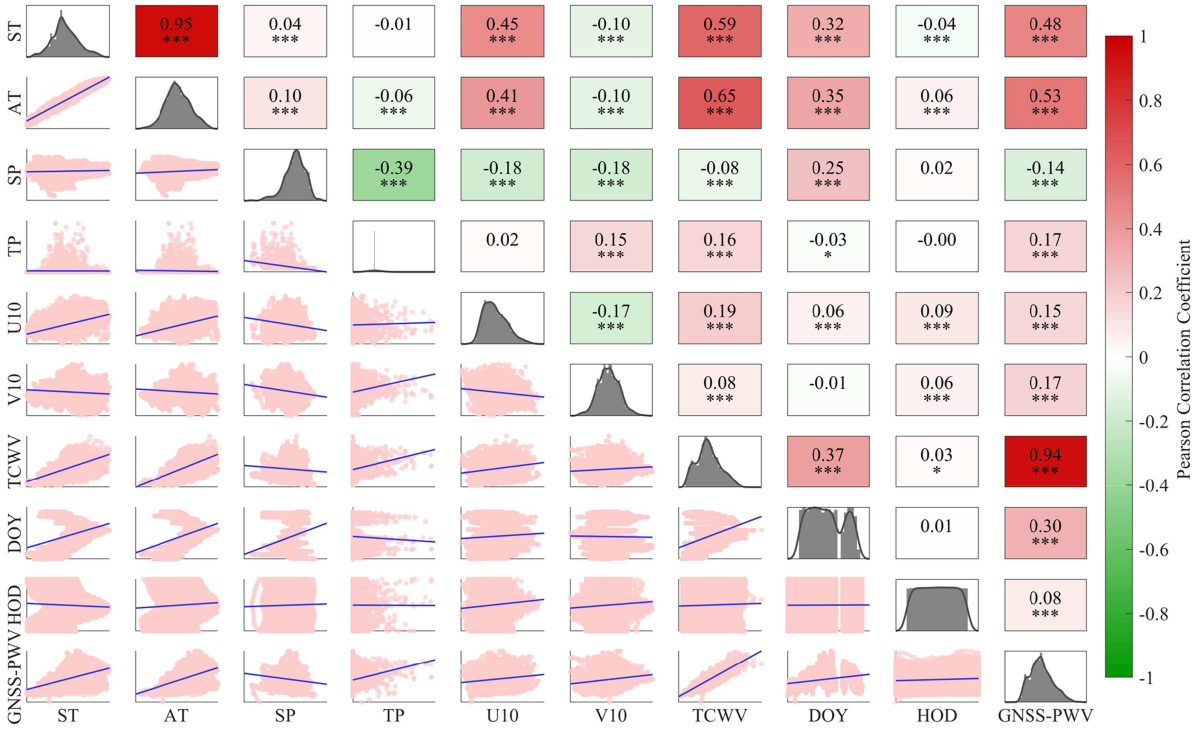

Figure 3. Correlations among meteorological elements, DOY, and HOD.

Table 3. The optional and optimal parameters for the RF and XGBoost algorithms.

Algorithm	Parameter	Optional values	Optimal value
RF	n_estimators	[100, 200, 300, 400, 500]	500
	max_depth	None	None
	min_samples_leaf	[1, 5, 10, 15]	1
	min_samples_split	[1, 5, 10, 15]	1
XGBoost	n_estimators	[100, 200, 300, 400, 500]	400
	max_depth	[1, 5, 10, 15]	15
	learning_rate	[0.001, 0.01, 0.1]	0.1
	min_child_weight	[1, 5, 10, 15]	1

TCWV, ST, AT, SP, TP, U10, V10, DOY, and HOD were used as input variables, while GNSS-PWV served as the output. The 75% of the data from 2022 to 2024 were randomly selected for model training, and the remaining 25% were used to test the model accuracy.

Hyperparameter selection is crucial to the performance, stability, and reliability of the modelling process and its results. A grid search with cross-validation (GridSearchCV) is used to determine the best optimised hyperparameters automatically. The hyperparameter settings for RF and XGBoost are listed in Table 3. Importantly, when the 'max_depth' of the RF is set to 'None', the decision tree continues to split nodes until each leaf is indivisible or contains fewer samples than 'min_samples_split'.

3.3. Accuracy evaluation

Figure 4 shows comparisons of the regionally calibrated ERA5-TCWV of 15 GNSS stations before and after using the RF and XGBoost algorithms. As shown in Figure 4(a2–b2), the relationships between the ERA5-TCWV and GNSS-PWV after RF and XGBoost calibrations are 0.98 and 0.99, respectively. Their biases are −0.01 and 0.01 mm, and their RMSEs are 1.32 and 1.15 mm, indicating RMSE improvements of 47.41% and 54.37% compared to the uncalibrated ERA5-TCWV (Figure 4(a1–b1)). The calibrated XGBoost-TCWV achieves higher accuracy than the RF-TCWV. It can be used to interpolate the missing GNSS-PWV data during earthquakes in the study region.

Figure 4 indicates that the calibrated ERA5-TCWV using the XGBoost algorithm exhibits higher accuracy. Table 4 lists the calibration accuracy of each GNSS station based on the XGBoost algorithm. The

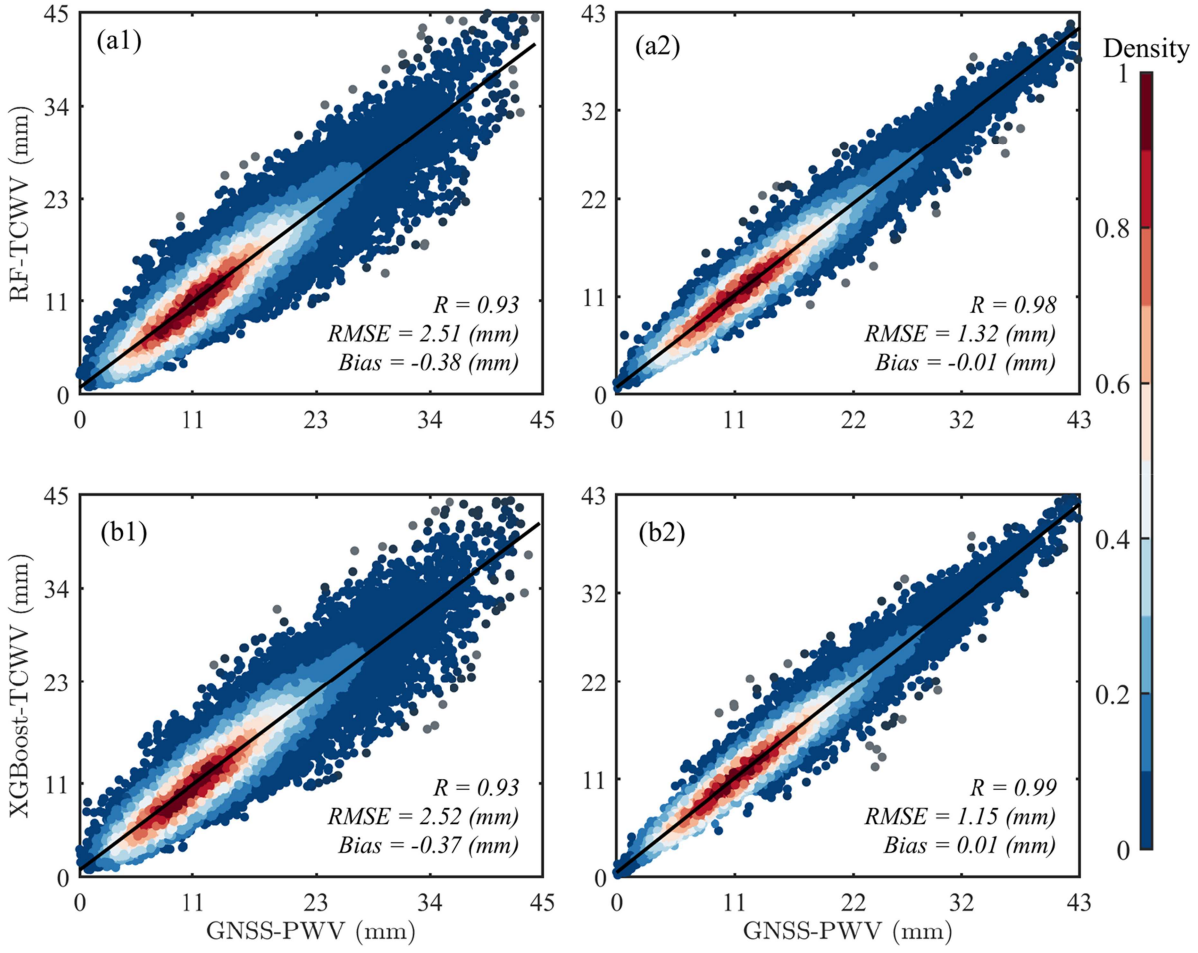

Figure 4. Comparisons of regional calibrated ERA5-TCWV of 15 GNSS stations before (a1–b1) and after (a2–b2) using RF and XGBoost algorithms.

Table 4. Accuracy of calibrated ERA5-TCWV using XGBoost algorithm at each GNSS station.

GNSS	R	RMSE	Bias
ANTP	0.97	0.79	0.00
KAHR	0.96	1.13	0.02
KLS1	0.97	0.96	0.01
ONIY	0.97	1.50	0.06
EKZ1	0.96	0.89	−0.00
FEEK	0.96	1.37	0.02
ADY1	0.96	1.09	0.03
TUF1	0.97	0.83	0.03
HAT2	0.96	1.36	0.00
ADN2	0.98	1.30	0.03
SURF	0.97	0.92	0.06
GURU	0.97	0.68	−0.02
MLY1	0.97	0.78	0.03
AKLE	0.97	1.02	0.03
POZA	0.97	0.95	0.03

GURU station has the highest accuracy, with an RMSE of 0.68 mm, whereas the ONIY station exhibits the lowest accuracy, with an RMSE of 1.50 mm.

4. Anomalies of multi-parameters

The displacements of the GNSS stations and multi-parameter anomalies of the surface, troposphere, and ionosphere are analysed in this section. Owing to data completeness on the day of the earthquake and page

limitations, four GNSS stations (ANTP, KLS1, TUF1, and ADN2) are selected to present the surface displacements and water vapour anomalies near the epicentres. The TEC anomalies are based on the UPC-derived GIM, which avoids potential GNSS data gaps. To ensure spatial representativeness across the study area, POZA, SURF, and the two epicentres (Mw 7.8 and Mw 7.5), which are located in different directions within the region, are selected for presentation.

4.1. Displacements

Figure 5 shows the displacements of four GNSS stations (ANTP, KLS1, TUF1, and ADN2) on Feb. 6. After the mainshock (Mw 7.8), the average displacements of 4 stations ranged from approximately ±8.53 cm in the east-west direction (E), ±12.15 cm in the north-south direction (*N*), and ±8.40 cm in the vertical direction (U). The largest displacement was observed at ANTP in the E direction, at ADN2 in the *N* direction, and at KLS1 in the U direction.

The subsequent largest aftershock (Mw 7.5) further magnified the displacement. In particular, the average displacement at the 4 stations expanded from ±8.5 cm to ±17.4 cm in the E direction, indicating greater crustal deformation in the E direction. Compared to the E direction, the average displacement amplitudes slightly decreased to ±9.4 cm and ±8.0 cm in the *N* and U directions, respectively. These findings suggest that the crust undergoes adjustment after continuous aftershocks. The most pronounced displacement was at ADN2 in the E and U directions and at TUF1 in the *N* direction. The mainshock (Mw 7.8) and aftershock (Mw 7.5) significantly altered the positions of the GNSS stations, and the resulting crustal displacements directly reflected the seismic rupture process.

During the earthquake gestation phase, long-term accumulation of crustal stress often led to upwelling of deep underground materials, accompanied by a series of geophysical and geochemical changes. When earthquake stress is released suddenly, a large amount of energy is emitted, causing not only obvious surface displacements, but also the release of significant quantities of greenhouse gases. The accumulation of crustal stress and the associated geophysical and geochemical variations can be transmitted to the upper atmosphere through the LAIC model (Tronin 2006). The land–atmosphere interactions and anomalies of multi-parameters from the land surface to the ionosphere are analysed in detail in the following sections.

4.2. ST, AT, SP, SLHF, and OLR of land surface

Figure 6(a,b) show the anomalies of ST and AT using the ZS method from Jan. 27 to Feb. 11, 2023 in the study region. The 10-day thermal anomalies of ST and AT observed before Feb. 6 were concentrated in two periods: from Jan. 27 to Feb. 1, and on Feb. 5. On Jan. 27, the maximum ZS values of ST and AT reached 3.56 and 3.97, respectively. The thermal anomalies were primarily distributed in the west of the epicentre. Subsequently, the thermal anomalies gradually intensified and expanded southeastward toward the epicentre. On Feb. 1, the maximum ZS values of the ST and AT reached 3.87 and 3.77, respectively, indicating widespread thermal anomalies in the southeast of the epicentre. Thereafter, their anomalies gradually weakened during Feb. 2–4. On Feb. 5, the maximum ZS values of the ST and AT increased to 3.52 and 4.14, respectively, with widespread thermal anomalies reappearing east of the epicentre. On Feb. 6, the maximum ZS values of ST and AT increased to 3.59 and 4.18, respectively, and the thermal anomalies continued. After Feb. 6, the thermal anomalies dissipated gradually.

Figure 6(c) shows the SP anomalies from Jan. 27 to Feb. 11, 2023 in the study region. Anomalous depressions dominated the study region during the 10 days before the earthquake, which were primarily concentrated in two periods: Jan. 29–Feb. 1 and Feb. 4–5. The minimum ZS of the SP from Jan. 29–Feb. 1 were −3.16, −5.00, −4.94, and −5.77, indicating persistent depression anomalies in the region. After Feb. 1, the depression anomalies weakened. During Feb. 4–5, the minimum ZS of the SP reached −2.52 and −7.35, and depression anomalies reappeared and intensified across the entire study region. On Feb. 6, the minimum ZS of the SP was −7.87, indicating a significant persistent depression anomaly. The depression anomaly continued on Feb. 7 but shifted to anomalously high pressure after Feb. 8.

Figure 6(d) shows the SLHF anomalies from Jan. 27 to Feb. 11, 2023 in the study region. Scattered SLHF anomalies were observed from Jan. 27 to Feb. 11. On Feb. 5, the day before the earthquake, the maximum ZS of the SLHF reached 20.03 in the east of the epicentre, representing the highest anomaly

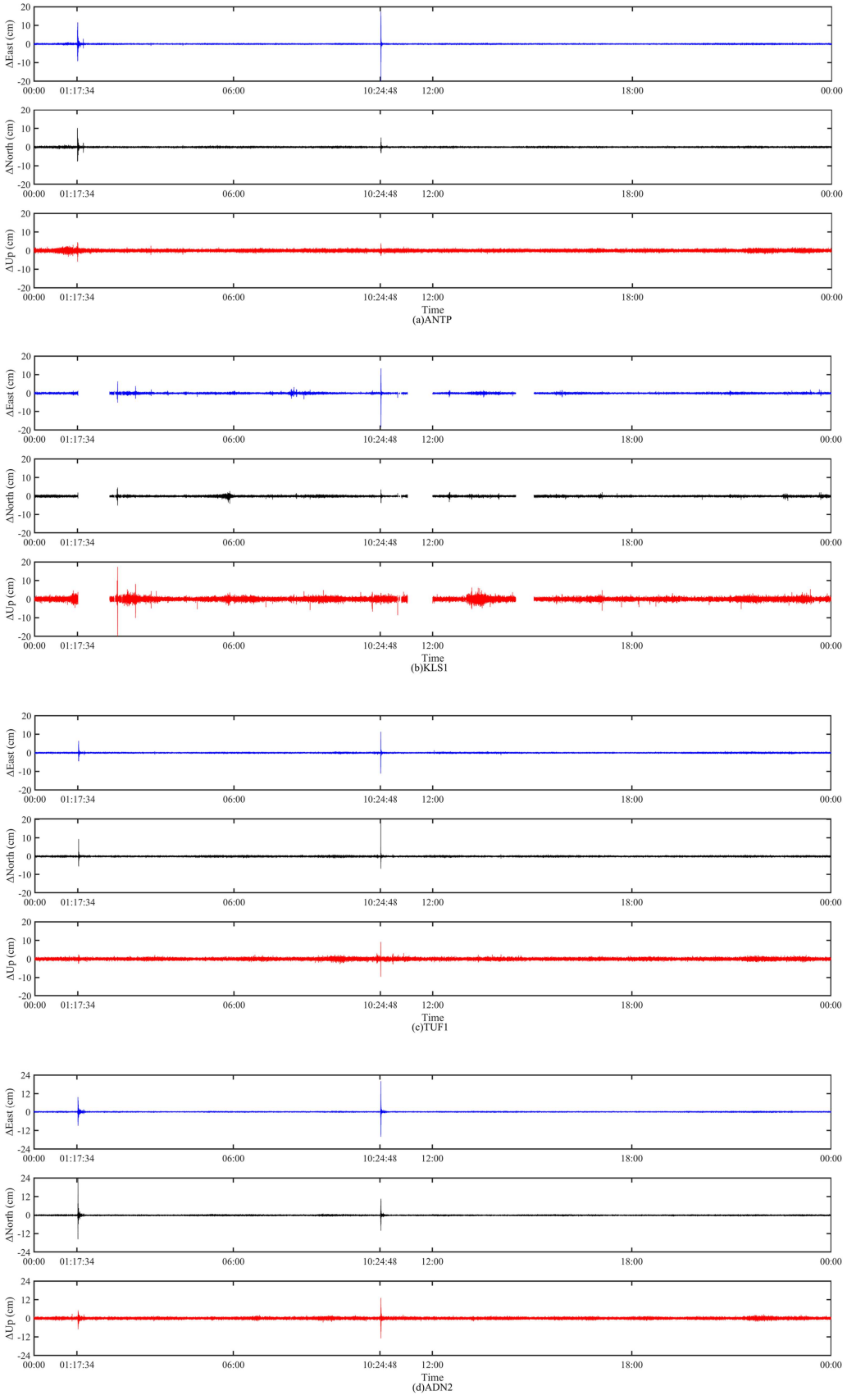

Figure 5. The station displacements of ANTP (a), KLS1 (b), TUF1 (c), and ADN2 (d) on Feb. 6, 2023.

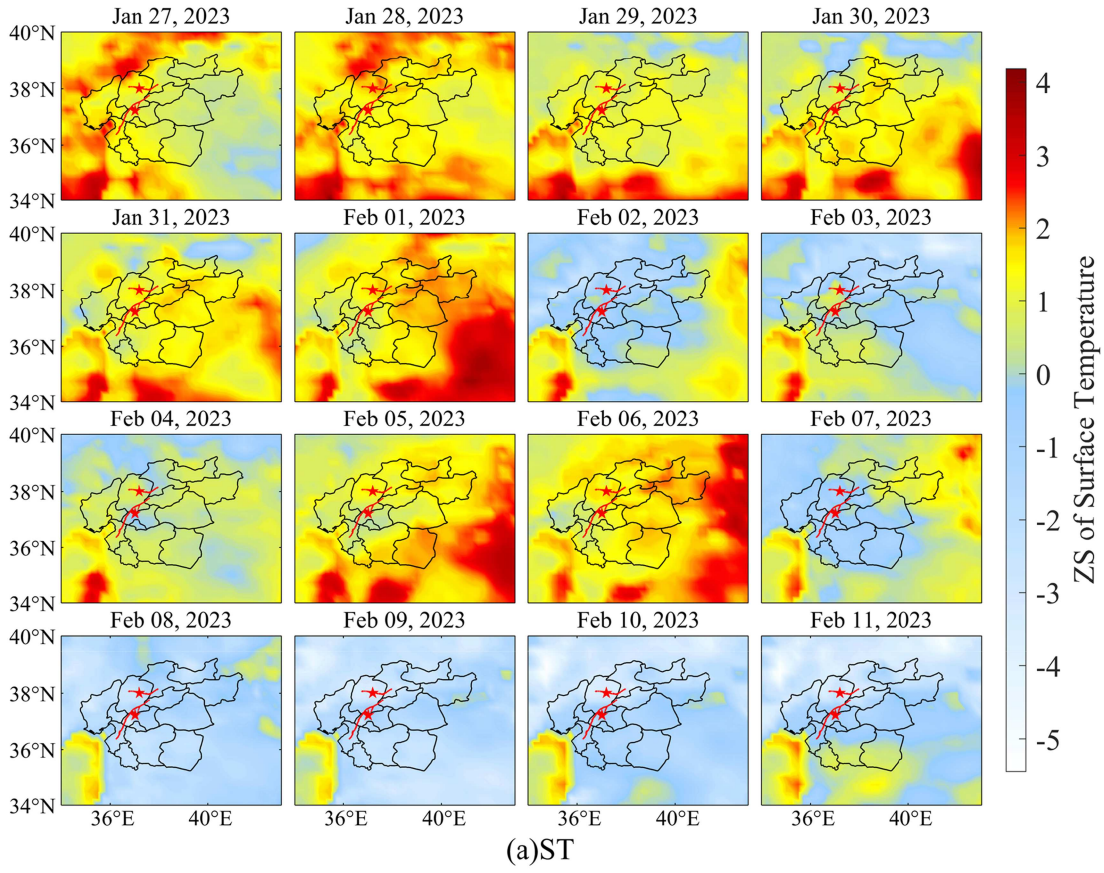

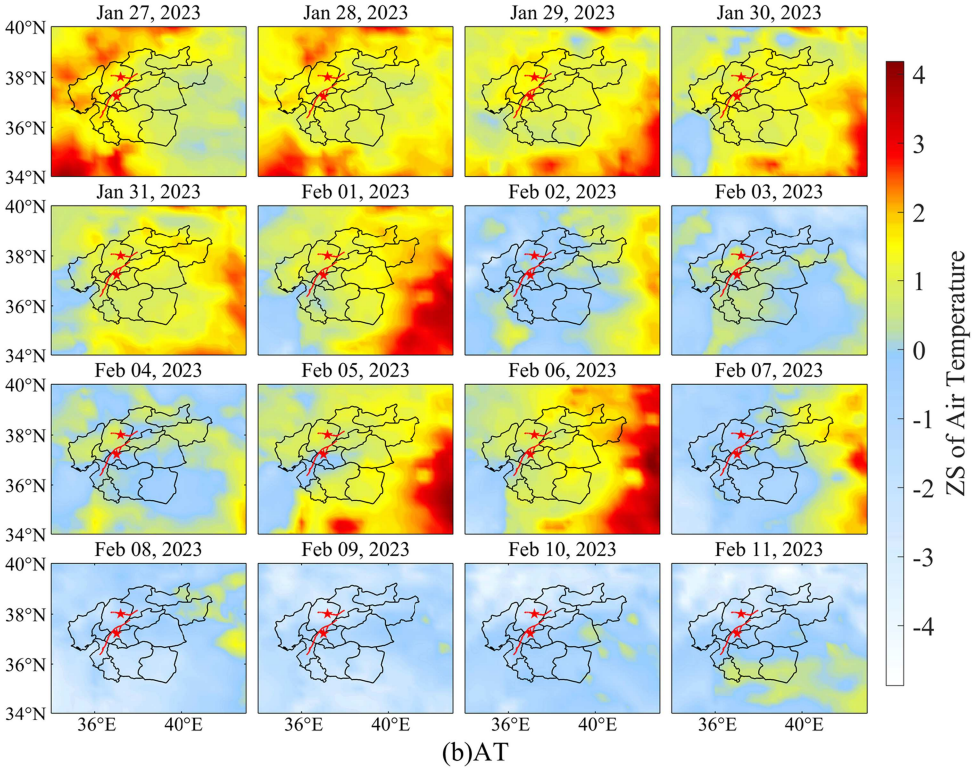

Figure 6. Anomalies of ST (a), AT (b), SP (c), SLHF (d), and OLR (e) from Jan. 27 to Feb. 11, 2023 in Turkey and Syria. (Red pentagrams indicate the epicentre; red lines represent faults.)

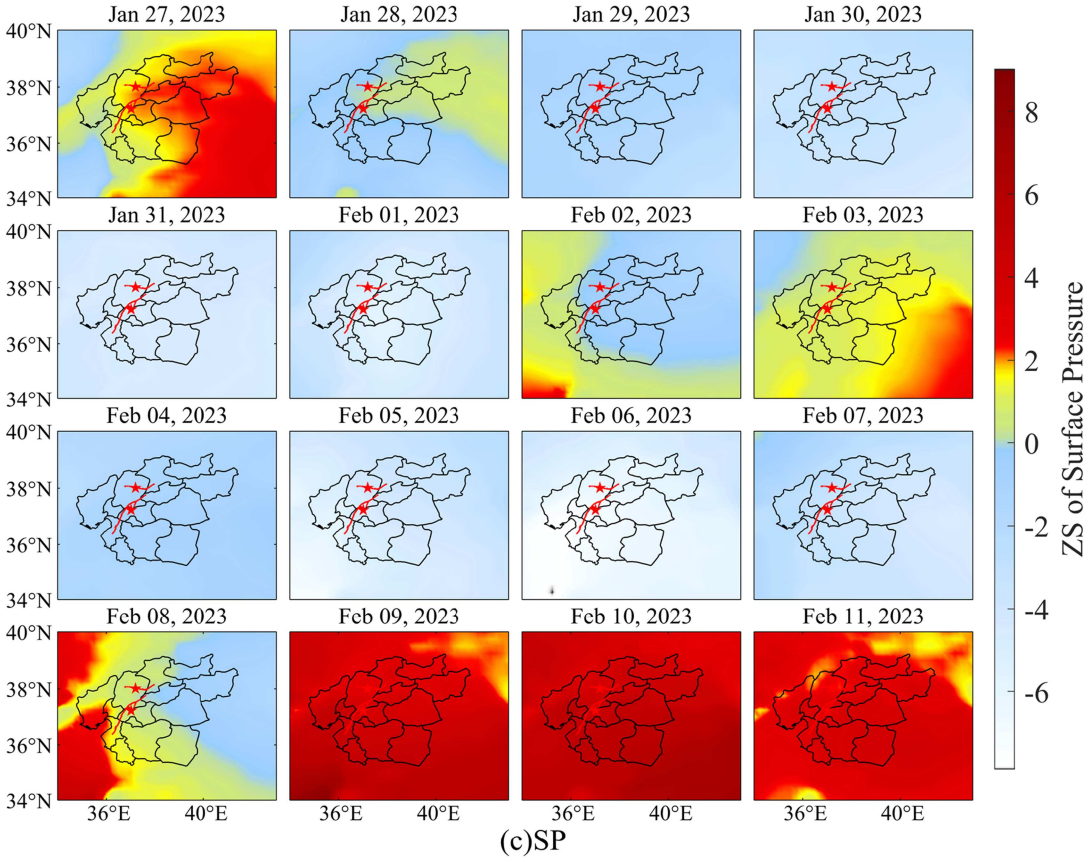

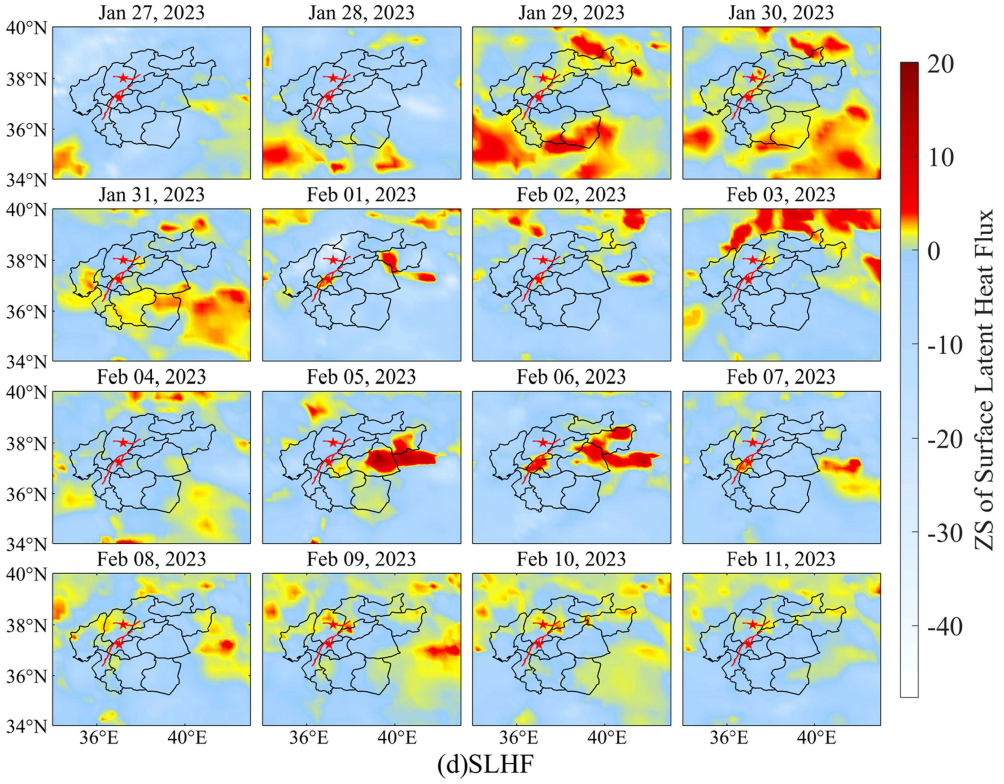

Figure 6. (*Continued*)

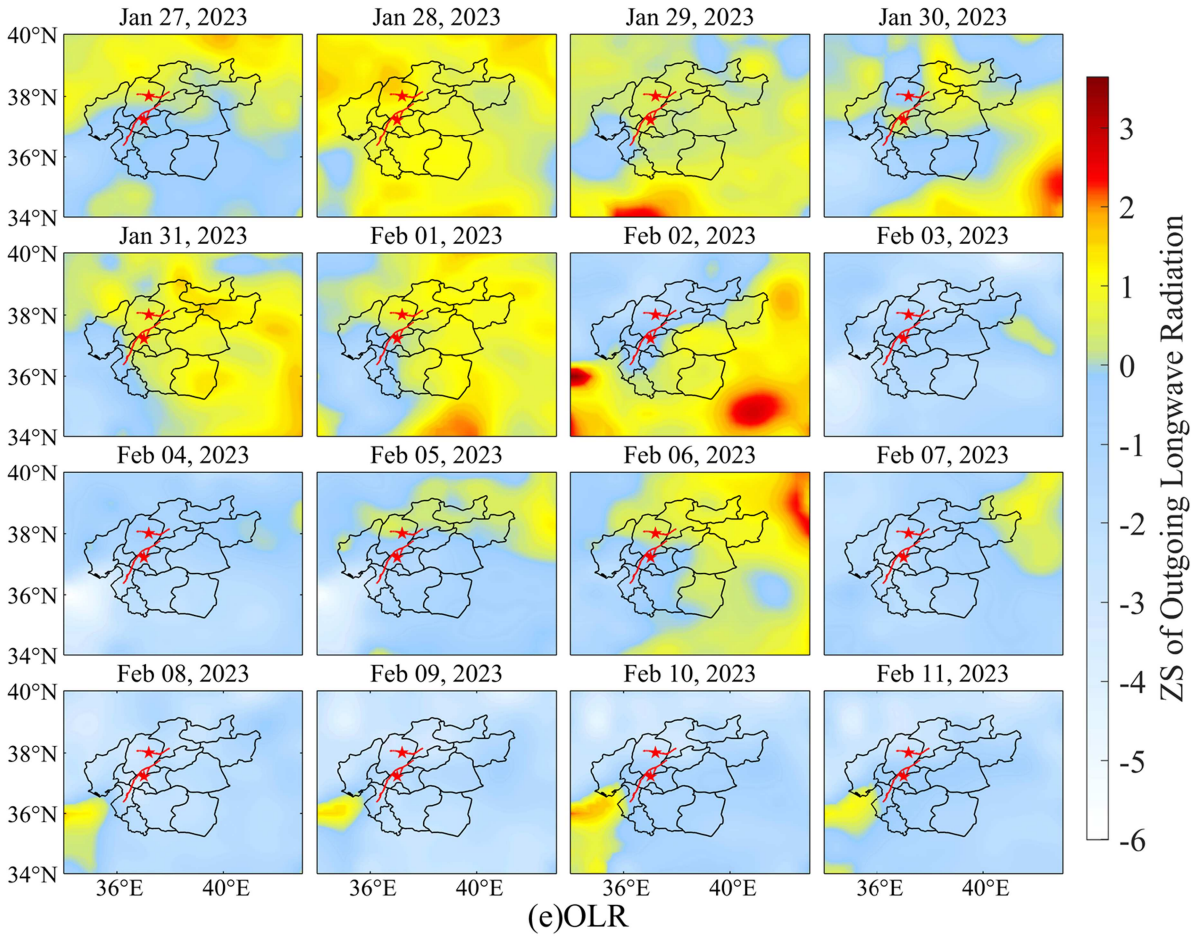

Figure 6. (*Continued*)

during the study period. On Feb. 6, high anomalies of SLHF reoccurred in the epicentral and eastern regions, with a maximum ZS of 13.03. After the earthquake, the SLHF anomalies weakened significantly, and only parts of the study region remained at high anomalies, which was possibly related to aftershocks.

Figure 6(e) shows the anomalies in the OLR from Jan. 27 to Feb. 11, 2023 in the study region. From Jan. 27 to Feb. 2, a positive ZS of the OLR was observed throughout the study region, indicating that the 2023 OLR exceeded the average of historical observations during the same period. However, a few parts of the epicentral southern region showed high anomalies of OLR on Jan. 29, Jan. 30 and Feb. 2, with maximum ZS indices of 2.54, 2.35, and 3.64, respectively. Anomalies gradually diminished after Feb. 2. On Feb. 6, a high anomaly was observed in the northeast of the epicentre, with a maximum ZS index of 2.46. After Feb. 6, the OLR anomalies gradually weakened and disappeared.

4.3. Water vapour

Figure 7 shows the TCWV anomalies from Jan. 27 to Feb. 11, 2023 in the study region. Higher TCWV anomalies occurred mainly during two periods: from Jan. 27 to Feb. 1 and on Feb. 5, the day before the earthquake. On Jan. 27, the maximum ZS of the TCWV was 3.48, and its water vapour anomalies were primarily distributed west of the epicentre. The anomalies subsequently intensified and extended to the southern region of the epicentre. On Jan. 30, the maximum ZS of the TCWV increased to 4.58, and widespread high anomalies appeared in the south of the epicentre. After Jan. 30, the anomalies expanded northeastward, and the maximum ZS of the TCWV reached 3.14 on Feb. 1, with other large-scale high anomalies. After its weakening during Feb. 2–4, the TCWV anomalies increased again on Feb. 5, with a

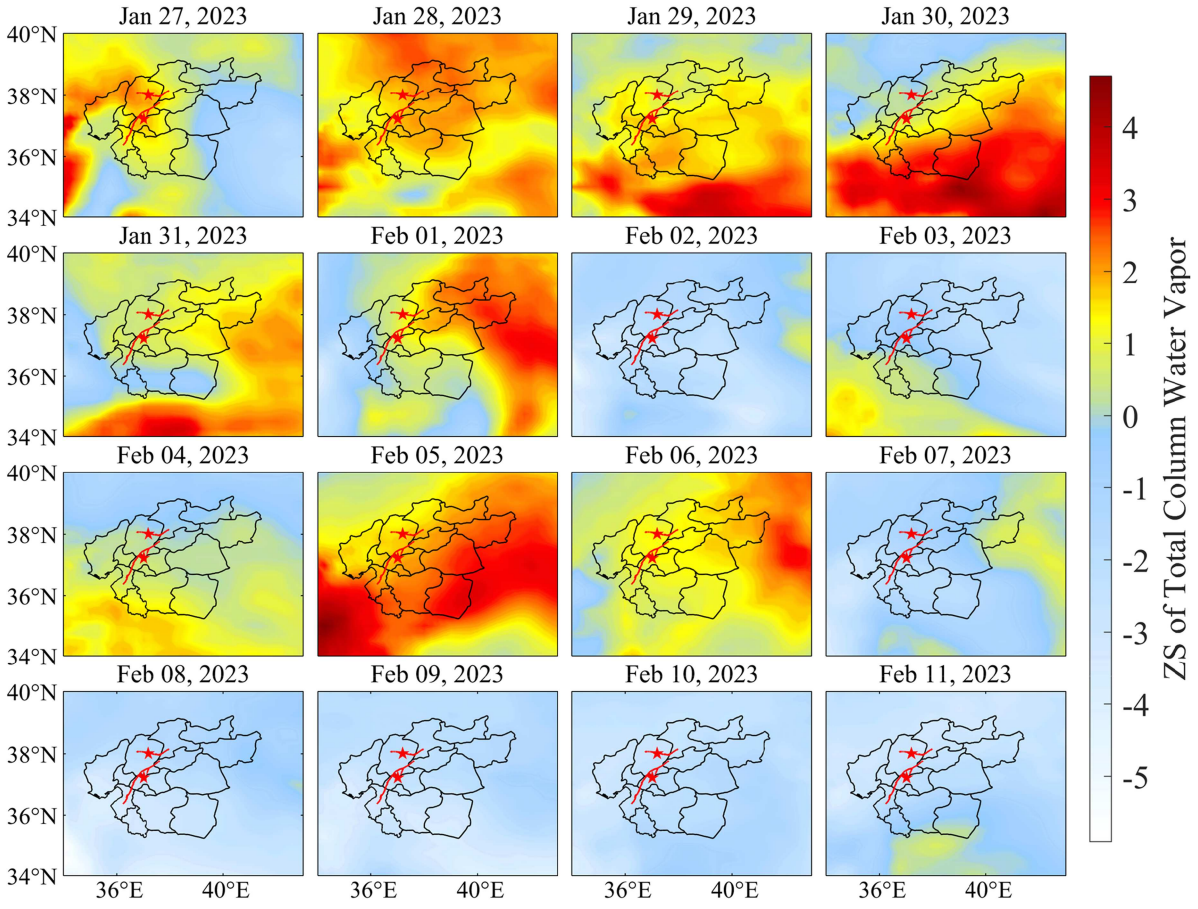

Figure 7. Anomalies of TCWV from Jan. 27 to Feb. 11, 2023 in the study region.

maximum ZS of 4.71, indicating another widespread anomaly in the study region. On Feb. 6, the maximum ZS of the TCWV was 3.02, and higher anomalies were maintained in the northeast region of the epicentre. After the earthquake, the anomalies weakened rapidly and gradually dissipated.

As shown in Figure 7 and Figure 6(a-b), the spatiotemporal water vapour anomalies are largely consistent with those of thermal anomalies during earthquakes. The slow creep of the underground faults released partial stress before the earthquake. Volatile gases, such as carbon dioxide, escape rock fractures. Violent crustal ruptures release substantial energy during earthquakes, leading to the formation of localised thermal anomalies. As the temperature of the land surface increased, the air temperature near the surface also increased, enhancing surface evaporation and the atmospheric water vapour content (Pulinets et al. 2006; Guo et al. 2023).

Figure 8 shows the Fourier spectral analysis of the TCWV from 2022 to 2024. Before the SIQR was used to detect anomalies of water vapour, it was essential to determine the width of the sliding window appropriately. An excessive window width may smooth abrupt signals and miss different climatic background fields or seasonal transitions. Conversely, a narrow window width tends to be overly sensitive for short-term fluctuations, misjudging diurnal variations as potential anomalies. Moreover, a narrower window width decreases the stability of quantile estimation, affecting the reliability of threshold determination.

As shown in Figure 8, the TCWV of ANTP, KLS1, TUF1 and ADN2 exhibit annual and semi-annual cycles, but their cycles of 365 days and 183 days are too large to be the window width. In the spectral range of 0–50 days, the TCWV of ADN2 and KLS1 showed a periodic fluctuation of approximately 20 days. Although the TCWV may be affected by solar radiation and temperature, resulting in diurnal variability in the study region, the overall diurnal cycle is small and does not represent the dominant periodic pattern. To ensure both the sensitivity of anomaly detection and the stability of estimation, the sliding window

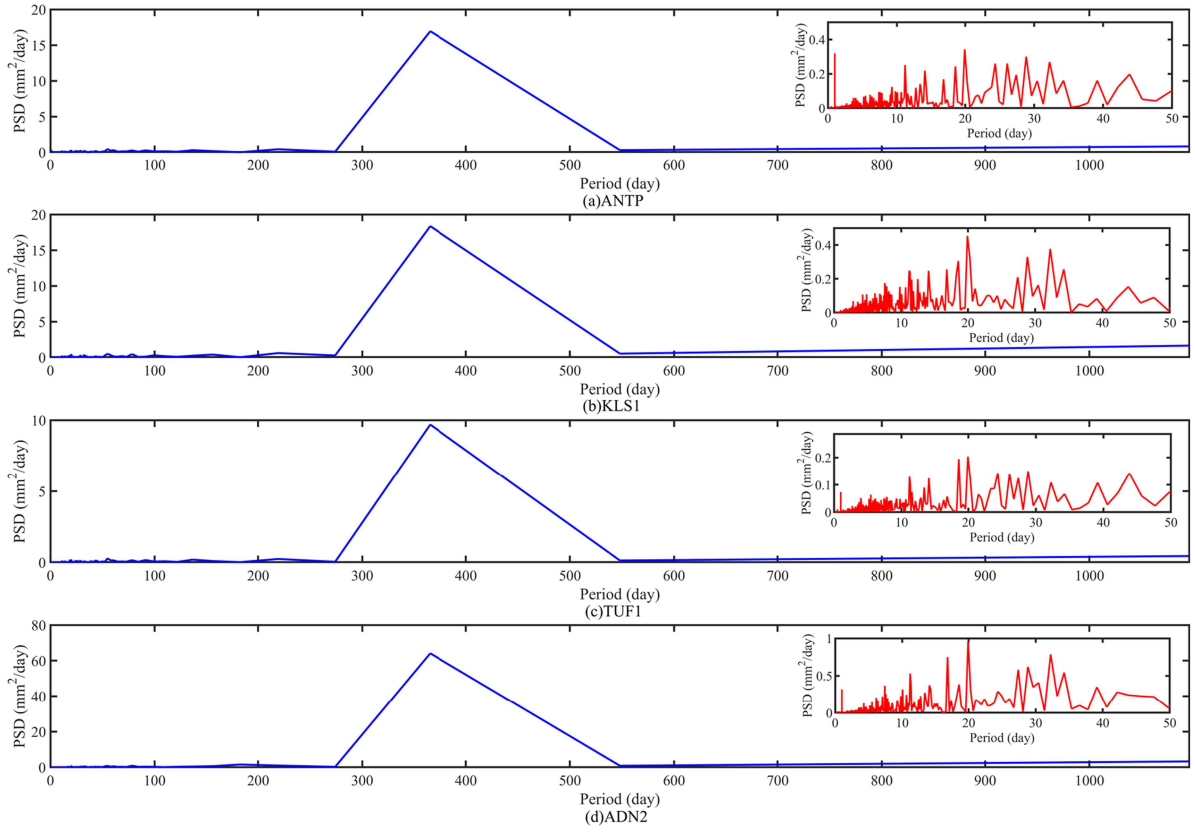

Figure 8. The spectral analysis of TCWV at ANTP (a), KLS1 (b), TUF1 (c), and ADN2 (d) stations during 2022–2024 using Fourier transform.

width for analysing water vapour anomalies using SIQR was set to 20 days in this study. The 20-day window width effectively captured the main fluctuation period and reduced the influence of periodic disturbances on the identification of anomalies, making it a reasonable and justified choice.

The ANTP station is closest to the epicentre (Mw7.8). It is taken as an example to select reasonable sliding window widths. Window widths of 10, 20, and 30 days were applied to analyse the PWV anomalies using the SIQR method during Jan. 27–Feb. 11, 2023 (Figure 9). The results indicate that, when a 10-day width is adopted, the SIQR method is highly sensitive to short-term fluctuations, identifying a large number of anomalies, some of which are actually noise. In contrast, when a 30-day width is used, the time series is substantially smoothed, reducing the number of anomalies. When a 20-day window is applied, pronounced anomalies are consistently detected during the two major PWV increases, and a minor anomaly is also identified during the major PWV decrease. These results further demonstrate the reasonableness and robustness of the 20-day sliding window width adopted in this study.

Figure 10 shows the anomalous variations of GNSS-PWV using SIQR at the ANTP, KLS1, TUF1, and ADN2 stations during Jan. 27–Feb. 11, 2023. Both ANTP and KLS1, which are closer to the epicentre, presented lower PWV anomalies on Feb. 2, with a maximum anomaly of −1.72 mm, and higher PWV anomalies on Feb. 5, with a maximum anomaly of 1.37 mm. On Feb. 6, a large number of higher PWV anomalies were detected at the ANTP between 00:00 and 07:00, with the largest anomaly reaching 2.99 mm 1 h before the earthquake occurred.

Notably, the PWV at the ANTP, KLS1, and TUF1 stations rapidly decreased 1 h before the mainshock and then quickly rose to a peak after the mainshock, forming a V-shaped variation pattern. From Jan. 27 to Feb. 6, anomalies of higher PWV at the ANTP station, which was closer to the epicentre, were detected twice, and anomalies of lower PWV were also detected. The PWV rapidly decreased by 2.12 mm, 7.20 mm, and 4.10 mm during 00:00–01:00. After the earthquake occurred, the PWV increased sharply. The PWV of

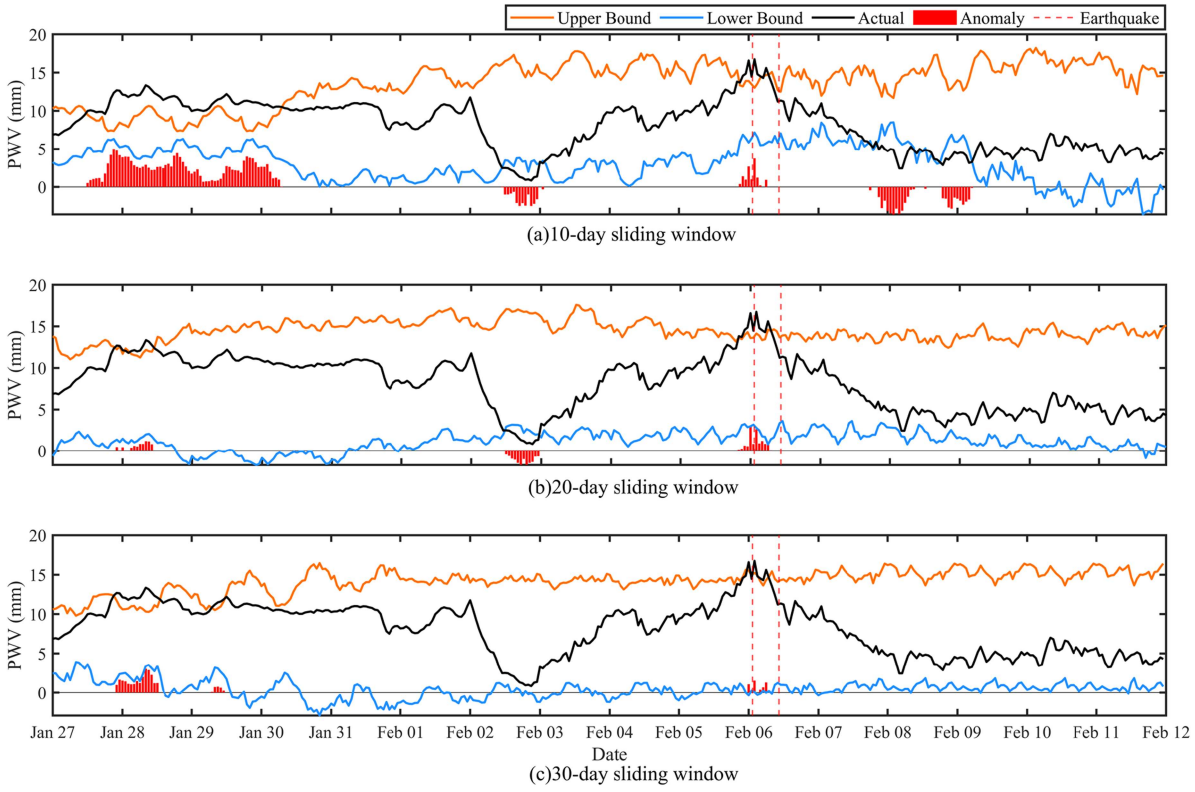

Figure 9. GNSS-PWV anomalies of 10-day (a), 20-day (b), and 30-day (c) window widths at ANTP during Jan. 27–Feb. 11, 2023.

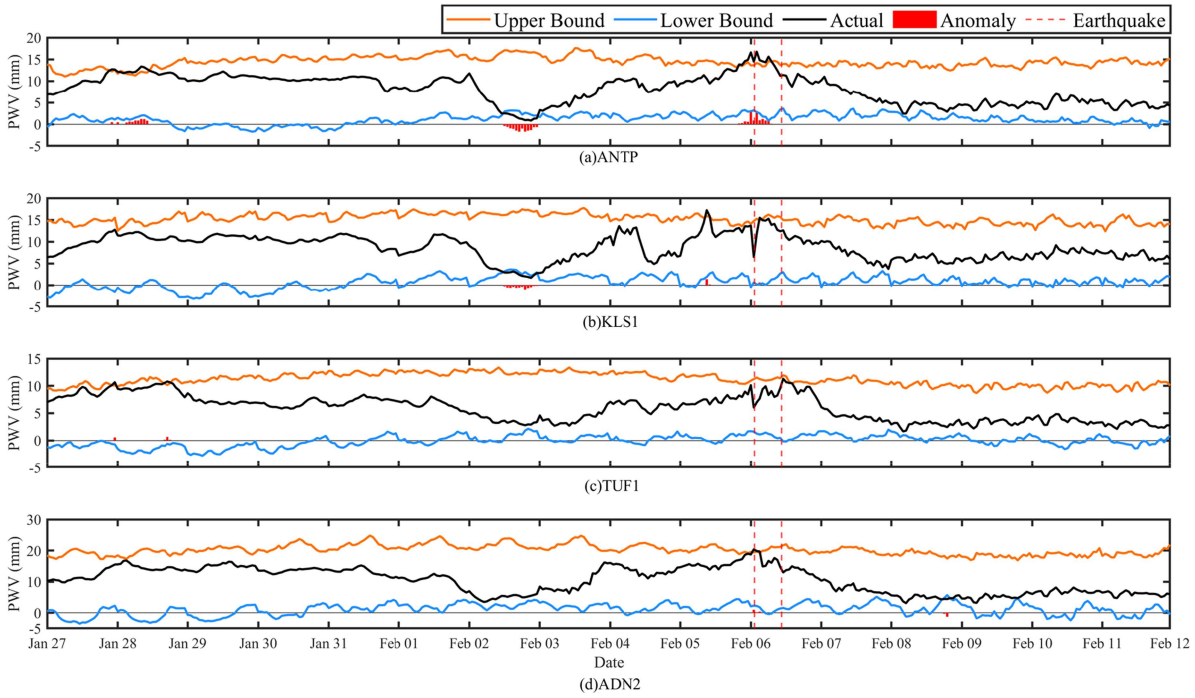

Figure 10. Anomalies of GNSS-PWV at ANTP (a), KLS1 (b), TUF1 (c), and ADN2 (d) stations during Jan. 27–Feb. 11, 2023 in the study region.

the ANTP increased by 2.29 mm between 01:00 and 02:00. The PWV of KLS1 increased by 9.02 mm between 01:00 and 03:00. The PWV of TUF1 increased by 3.90 mm between 01:00 and 05:00.

According to Figure 10 and Table 1, the PWV increases more rapidly when the GNSS stations are closer to the epicentres, and a higher PWV peak is also observed after the mainshock. Conversely, the PWV increases more slowly when the GNSS stations are far from the epicentres. The increasing characteristics of the PWV suggest that the earthquake-released energy propagates to the atmosphere with a delay, resulting in a noticeable time lag in the response to atmospheric water vapour disturbance. However, the PWV peak at ADN2 appeared between 00:00 and 01:00, decreased later, and did not rebound significantly after the mainshock. This PWV phenomenon at ADN2 may be attributed to its long distance (152.34 km) from the epicentre (Mw 7.8) and low altitude (69.30 m).

4.4. Total electron content

Figure 11 shows the variations in geomagnetic and solar activity indices during Jan. 27–Feb. 11, 2023. As shown in Figure 11, Kp*10 was below 40, Dst was above −50, and Ap was lower than 20 before Feb. 6, indicating weak geomagnetic activity. F10.7 reached 140.5 and 140 on Jan. 27 and Feb. 5, whereas it remained below 140 during other periods, suggesting low solar activity. These indices indicate that geomagnetic and solar activities were relatively quiet, causing minimal disturbance to the ionospheric TEC before Feb. 6.

On Feb. 6, Kp*10 was under 40, Dst was above -50, and Ap reached 22 only between 18:00 and 23:00, indicating weak geomagnetic activity. F10.7 increased to 152.4, reflecting a slight increase in solar activity with a limited amplitude. After Feb. 6, the geomagnetic and solar activity indices increased gradually. The Dst was above −50, but the Kp*10 exceeded 40 at certain periods on Feb. 9, and the Ap exceeded 20 several times during Feb. 7–10, demonstrating a significant enhancement of geomagnetic activity. F10.7 was above 179.7, indicating an obvious increase in solar activity after Feb. 6. The ionosphere may have been jointly influenced by solar and geomagnetic activities after Feb. 6.

Geomagnetic and solar activities, together with the ionospheric TEC, exhibit clear multi-scale periodicities that reflect the complex energy transfer and coupling within the Sun–Earth system. Solar activity shows several characteristic periods, including the 11-year Schwabe cycle, the 22-year Hale cycle,

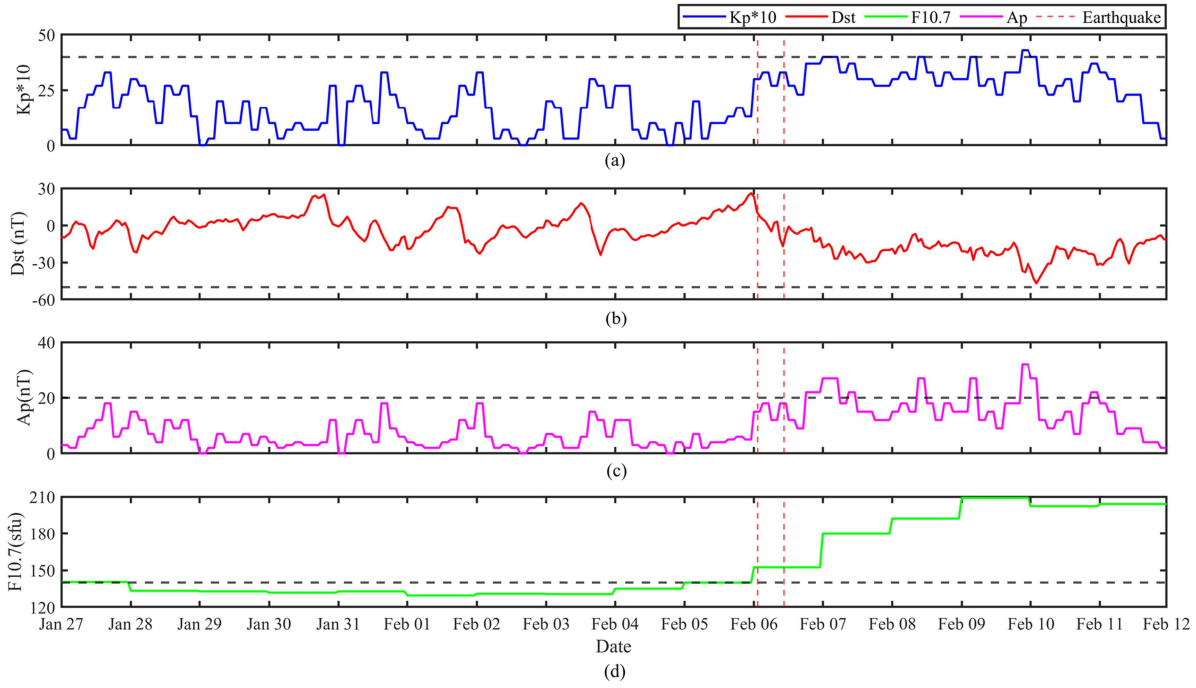

Figure 11. Temporal variations of geomagnetic and solar activity indices during Jan. 27–Feb. 11, 2023.

the 80- to 100-year Gleissberg cycle, a 1.3- to 1.7-year quasi-periodic oscillation, and the 27-day solar rotation period with its 13.5-day harmonic (Kotzé 2016; Vecchio et al. 2017). Geomagnetic activity is modulated by solar radiation and solar wind, showing cycles consistent with 11- and 22-year solar cycles, semi-annual variations, 27-day and 13.5-day rotation-related cycles, and a 1.3- to 2.9-year quasi-biennial oscillation (Kane 1997). TEC variations are influenced by solar activity and magnetosphere–ionosphere coupling, exhibiting long-term 11-year modulation, semi-annual (spring and autumn) peaks, diurnal variations, and 27- and 13.5-day oscillations (Feng et al. 2023). These patterns indicate that the ionosphere responds to solar and geomagnetic disturbances across multiple time scales.

As discussed in Section 4.3, the sliding window width in the SIQR should be neither too large nor too small. Therefore, in this study, 27 days were used, which not only allows for the extraction of periodic signals associated with solar and geomagnetic activities, but also effectively minimises their interference in detecting TEC anomalies.

The inverse distance weighting method was applied to interpolate the TEC grid data to the epicentres (Mw 7.8 and Mw 7.5), as well as to the POZA and SURF stations. As shown in Figure 12, low TEC anomalies were detected at four locations at 16:00 and 17:00 on Feb. 4, with a maximum of 1.61 TECU. On Feb. 5, TEC anomalies appeared at 17:00, 19:00, and 22:00 at the epicentre (Mw 7.8); at 19:00, 22:00, and 23:00 at the epicentre (Mw 7.5); at 19:00, 21:00, and 22:00 at the ANTP station; and at 16:00, 17:00, and 22:00 at the SURF station. However, these anomalies were low, with a maximum of 1.42 TECU. On Feb. 6, TEC anomalies were detected at all four locations except at 07:00 and 08:00, with a maximum anomaly of 14.83 TECU. During Feb. 7–11, numerous TEC anomalies were observed at all locations, with a maximum anomaly of 11.07 TECU.

Based on the analysis of Figures 11 and 12, the geomagnetic and solar activities were relatively quiet, causing minimal disturbance to the ionospheric TEC before Feb. 7. Therefore, the TEC anomalies observed on Feb. 4–5 may have been related to the impending earthquake. On Feb. 6, the geomagnetic

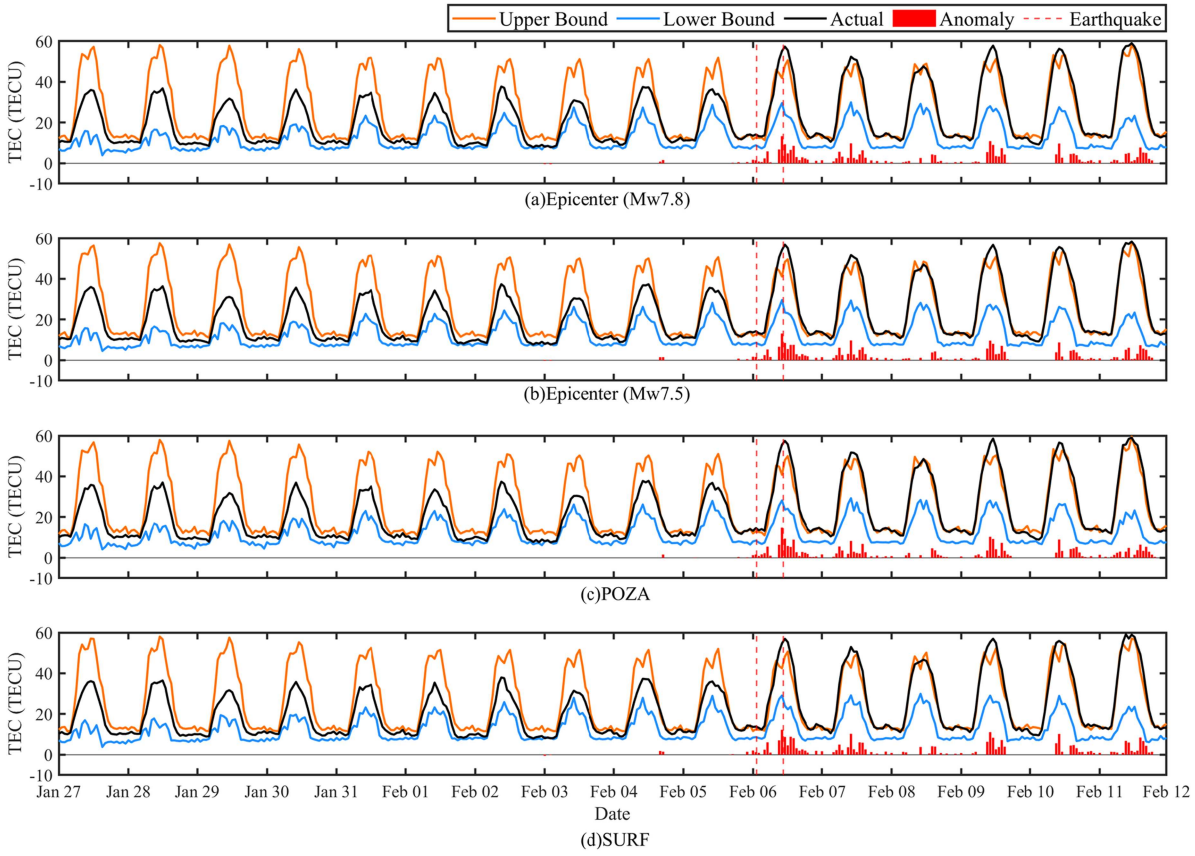

Figure 12. The TEC anomalies of epicentres (Mw 7.8 and Mw 7.5), POZA and SURF stations during Jan. 27–Feb. 11, 2023.

activity was weak, the solar activity increased slightly, and TEC anomalies were more likely to have been induced by the earthquake. After Feb. 6, the TEC anomalies increased, while geomagnetic and solar activities also intensified. This finding indicates that the observed increase in TEC anomalies is consistent with and likely influenced by enhanced geomagnetic and solar activities, though a contributory role of post-seismic processes cannot be entirely ruled out without further analysis.

Figure 13 shows the spatial distributions of the TEC on Feb. 6. After 4:00, the TEC gradually increased from east to west. A wide range of higher TEC emerged at 11:00 and 12:00, with a maximum of 56.90 TECU and 60.80 TECU, respectively. Subsequently, the higher TEC region continued to spread westward. Until 13:00, a decreasing trend is observed from west to east. Until 23:00, the TEC decreased significantly, with a maximum TEC of 16.00 TECU. The TEC variations were consistent with the solar activity patterns, with higher TEC values corresponding to intensified solar activity between 11:00 and 13:00.

Combined with Figures 13 and 14, the maximum TEC reached 40 TECU before Feb. 6, while the maximum TEC rose significantly to 60.80 TECU on Feb. 6. The Ap reached 22 between 18:00 and 23:00 on the same day, without causing notable TEC disturbances. Meanwhile, F10.7 reached 152.4, indicating a modest increase in solar activity, which was insufficient to explain the higher TEC on Feb. 6. Considering the relatively modest geomagnetic and solar activities, a higher TEC is likely to be highly associated with seismic activity on Feb. 6.

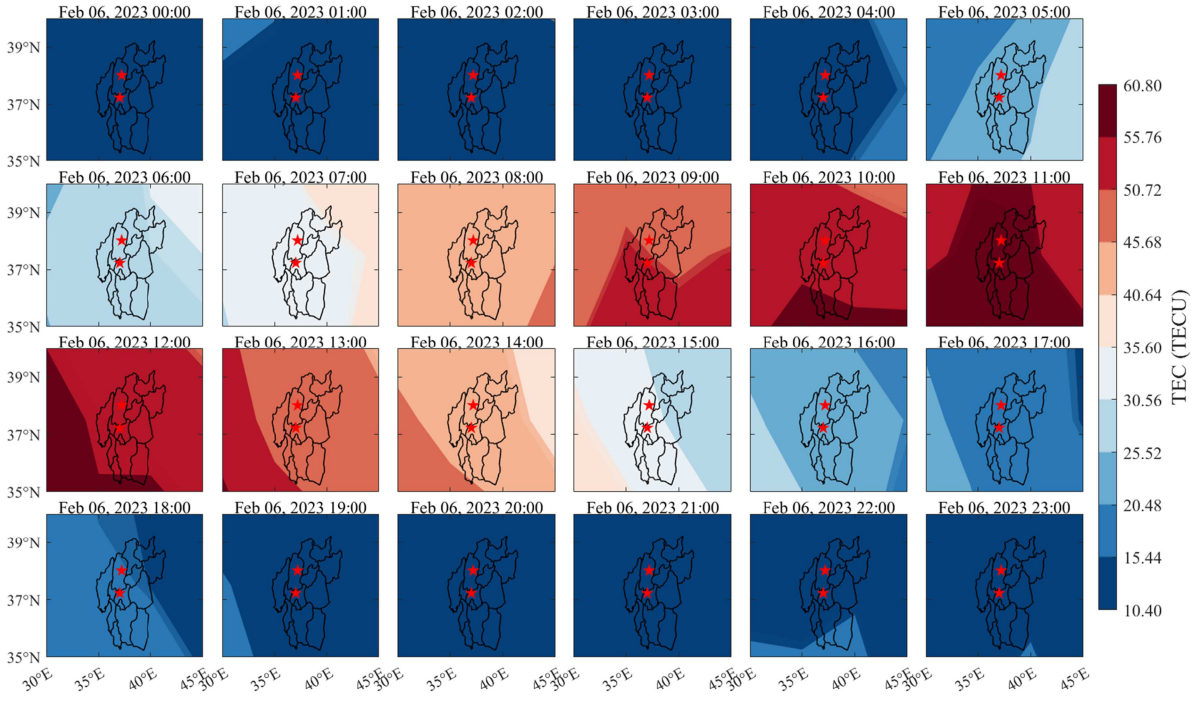

Figure 13. The spatial TEC variations in the study region on Feb. 6, 2023.

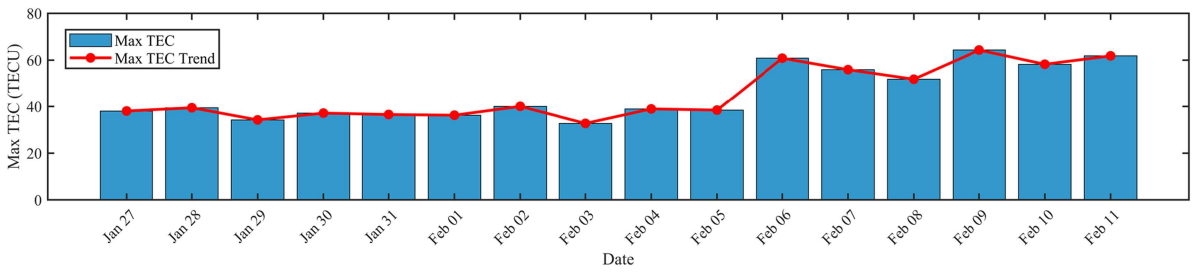

Figure 14. The daily maximum TEC in the study region during Jan. 27–Feb. 11, 2023.

5. Discussion and conclusions

Figure 15 shows the daily extreme ZS of land-atmospheric multi-parameters in the study region during Jan. 27–Feb. 6, 2023. The daily maximum ZS of SLHF and TCWV reached 20.03 and 4.71, respectively, on Feb. 5, indicating a significant release of surface energy and notable accumulation of water vapour in the lower atmosphere. On Feb. 6, the ZS of AT achieved a daily maximum of 4.18, whereas the ZS of SP reached a daily minimum of −7.87, indicating a significantly high-temperature and low-pressure environment.

Table 5 presents the anomalous periods and corresponding land–atmosphere multi-parameter extremums identified by different detection methods from Jan. 27 to Feb. 6, 2023. Two main anomalous periods are observed: Jan. 27–Feb. 1 and Feb. 5–6. Figure 15 and Table 5 show that the study area is characterised by high temperature, high water vapour, low pressure, and high TEC during these periods, reflecting a distinctive land–atmosphere environmental conditions.

In a previous study (Ma et al. 2025), surface temperature and atmospheric water vapour anomalies associated with 12 earthquakes (Mw ≥ 5.0) in the Asia–Pacific region were analysed systematically. The data of surface temperature, GNSS-ZTD, and precipitation 10-day before and 5-day after each earthquake were used to identify and analyse anomalies in thermal and water vapour based on the methods of Z-Score and wavelet transform. The results indicated that pronounced surface temperature anomalies were commonly observed within the $5° \times 5°$ epicentre region. The thermal anomalies were predominantly concentrated near the epicentres and generally preceded the corresponding water vapour anomalies. Moreover, the D4 high-frequency wavelet components of GNSS-ZTD exhibited significant fluctuations within 1–3 days before and after the earthquakes, suggesting intensified water vapour activities. These results provide important empirical findings of the LAIC mechanism associated with the Turkey earthquakes in this study.

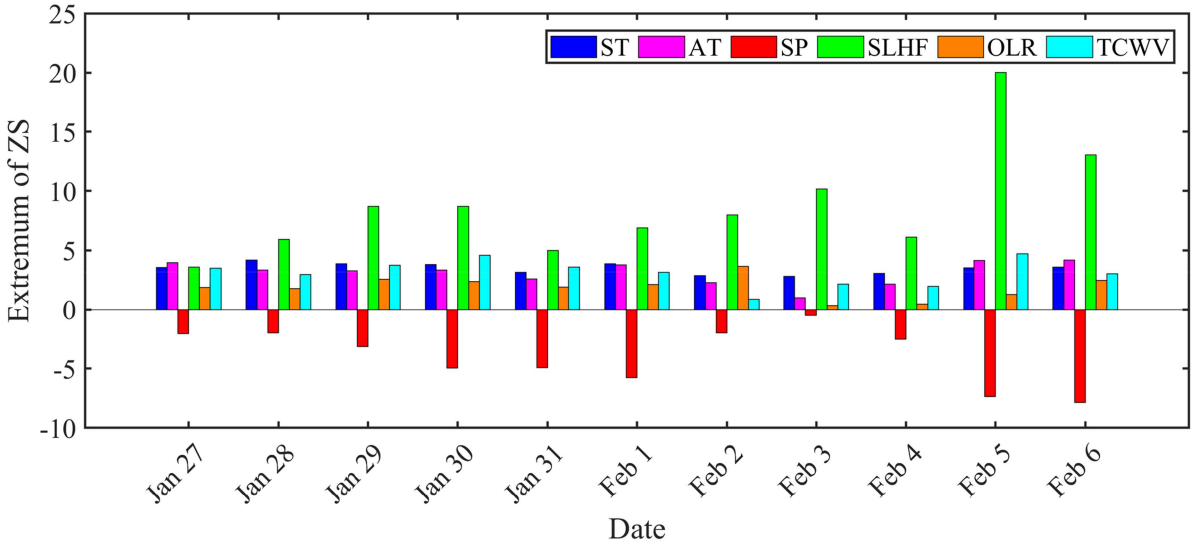

Figure 15. The ZS extremums of ST, AT, SP, SLHF, OLR, and TCWV in the study region during Jan. 27–Feb. 6, 2023.

Table 5. Summary of different detection methods from Jan. 27 to Feb. 6, 2023.

Parameter	Method	Anomaly	Period	Maximum anomaly
ST	Z-score	Positive	Jan. 27–Feb. 1; Feb. 5–6	3.87
AT	Z-score	Positive	Jan. 27–Feb. 1; Feb. 5–6	4.18
SP	Z-score	Negative	Jan. 29–Feb. 1; Feb. 4–6	−7.87
SLHF	Z-score	Positive	Feb. 5–6;	20.03
OLR	Z-score	Positive	Jan. 27–Feb. 2; Feb. 6	3.64
TCWV	Z-score	Positive	Jan. 27–Feb. 1; Feb. 5–6	4.71
PWV	SIQR	Negative; Positive	Feb. 2; Feb. 5–6	−1.72 mm; 2.99 mm
TEC	SIQR	Positive	Feb. 4–6	14.83 TECU

With respect to the TEC anomalies, the Turkey (Mw 7.8) earthquake was compared with the Lorca, Spain, earthquake (Mw 5.1) and the Ain Témouchent, Algeria, earthquake (Mw 5.7) (Tachema et al. 2022; Tachema 2024). Table 6 summarises their magnitudes, tectonics, data sources, methods, and study periods. The pre- and post-seismic ionospheric TEC anomalies of the three earthquakes were observed. However, some of the research results differ because different data sources, data processing methods and data spans are used for each earthquake. In future research, consistent data sources, spans, and methods should be adopted to systematically compare the TEC anomalies of earthquakes of different magnitudes and obtain more reliable conclusions.

Before an earthquake, the slow creep of underground faults releases part of the strain energy and converts it into land heat (Ortega-Arroyo et al. 2025). This process emits greenhouse gases such as radon and carbon dioxide, enhancing local radiative energy and surface temperature (D'Incecco et al. 2021). Subsequently, the significant increase in SLHF resulted in the transportation of atmospheric water vapour and an increase in the TCWV. The local water vapour accumulated, and the air humidity increased, destabilising the atmospheric structure, leading to a decrease in surface pressure. When atmospheric water vapour reaches saturation after vertical convection and condenses into droplets, resulting in precipitation and the release of latent heat, it further promotes the upward propagation of local convective disturbances along gravity waves or electrostatic fields. This process may influence the higher atmospheric layers, up to the ionosphere.

The aforementioned earthquake procedure manifests as a complete evolutionary chain: surface warming, surface depression, water vapour accumulation, precipitation occurrence, temperature reduction, and ionospheric disturbance, providing physical evidence for the lithosphere–atmosphere–ionosphere coupling mechanism. Specifically, SLHF and TCWV anomalies occurred one day prior to the earthquake, reflecting significant changes in energy and water vapour within the lower atmosphere. The rising AT and falling SP further reveal the upward transmission of local thermal disturbances. Energy propagation aligns with the LAIC mechanism, which describes the chain mechanism whereby crustal thermal anomalies trigger disturbances in the troposphere and ionosphere (Pulinets and Ouzounov 2011).

Multi-source data of GNSS, ERA5, geomagnetic and solar activity indices, and TEC data from the 2023 Turkey earthquake were utilised in this study. The accuracy of the ERA5-TCWV was evaluated, and two GNSS-PWV interpolation models were developed using the RF and XGBoost algorithms. The displacement characteristics of the 15 stations were analysed using GNSS on the day of the earthquake. The anomalous variations in land–atmospheric multi-parameters from the land surface, near-surface, troposphere, and ionosphere during the earthquake were analysed using SIQR and ZS methods. The main conclusions are as follows:

(1) The RMSE between the ERA5-TCWV and GNSS-PWV of 15 GNSS stations ranged from 1.47 mm to 4.80 mm, with an average of 2.33 mm, indicating that the ERA5-TCWV should be calibrated with GNSS-PWV. The RMSE of the calibrated ERA5-TCWV using the RF and XGBoost algorithms decreased significantly to 1.32 mm and 1.15 mm, respectively. These methods are suitable for interpolating missing GNSS-PWV data before and after the Turkey earthquake in 2023.
(2) After the Turkey mainshock (Mw 7.8), the average surface displacements at four GNSS stations (ANTP, KLS1, ADN2, and TUF1) were approximately ±8.53 cm, ±12.15 cm, and ±8.40 cm in the E, N, and U directions, respectively. The aftershock (Mw 7.5) increased the average surface displacement to ±17.42 cm in the E direction. The average displacements reached ±9.43 cm and ±7.98 cm in the *N* and U directions, respectively.

Table 6. The summary of Lorca, Spain, Ain Témouchent, Algeria, and Turkey earthquakes.

Item	Lorca, Spain	Ain Témouchent, Algeria	Turkey
Mw	5.1	5.7	7.8
Tectonics	Shallow-focus left-lateral strike-slip fault (Alhama–de Murcia) with compression	Reverse fault; located at the African–Eurasian convergence zone	Left-lateral strike-slip; East Anatolian Fault under Arabian–Eurasian compression
TEC	TEC maps generated from GNSS-TEC	TEC maps generated from GNSS-TEC	UPC-derived GIM
Resolution	5° lon × 2.5° lat, 2-h	5° lon × 2.5° lat, 2-h	5° lon × 2.5° lat, 1-h
Method	Wavelet transform	Residual Anomaly	SIQR
Span	Apr. 1–Jun. 1, 2011	Sep. 15, 1999–Feb. 1, 2000	Jan. 27–Feb. 11, 2023

(3) Anomalous variations in the land surface, near-surface, and troposphere before the earthquake were concentrated primarily from Jan. 27 to Feb. 1 and Feb. 5–6. High temperature and low pressure were the main pre-earthquake environmental characteristics. The ZS values of the SLHF and TCWV reached their maximum of 20.03 and 4.71, respectively, one day before the earthquake. The ZS of AT achieved a maximum of 4.18 on Feb. 6, while the ZS of SP reached its minimum of −7.87. The PWV displayed a distinct V-shaped variation pattern. It decreased rapidly 1 h before the earthquake and rose quickly to its peak after the earthquake. The ANTP station near the epicentre detected a high PWV anomaly (2.99 mm) one hour before the earthquake, which exceeded the maximum anomaly from Jan. 27 to Feb. 1.

(4) Based on the SIQR method, low TEC anomalies were detected on Feb. 4–5, with a maximum of 1.61 TECU. Numerous TEC anomalies were identified on the day of the earthquake, and subsequently, the largest anomaly reached 14.83 TECU. Based on the analysis of solar and geomagnetic activities concurrently, it is suggested that the anomalies observed before and on the day of the earthquake were likely related to the seismic event. However, the anomalies observed after the earthquake may be related to enhanced geomagnetic and solar activities, or possibly to the earthquake itself, and further research is required to clarify their causes.

Acknowledgements

The authors would like to express their sincere gratitude to the U.S. Geological Survey (USGS) for providing the earthquake data, TUSAGA-Aktif and Nevada Geodetic Laboratory for providing the GNSS data, Copernicus Climate Change Service for the reanalysis data, NASA OMNIWeb service for the geomagnetic and solar activity indices, and NASA CDAWeb for the TEC data.

Author contributions

CRediT: **Li Li:** Conceptualization, Funding acquisition, Investigation, Methodology, Project administration, Resources, Writing – original draft, Writing – review & editing; **Huafeng Ma:** Conceptualization, Data curation, Formal analysis, Methodology, Software, Validation, Visualization, Writing – original draft; **Galina Dick:** Funding acquisition, Project administration, Supervision; **Jens Wickert:** Funding acquisition, Project administration, Supervision, Writing – review & editing; **Enchen Wu:** Methodology, Software, Visualization; **Mingsong Zhang:** Software, Validation, Visualization; **Zehua Meng:** Software, Visualization; **Yuqing Huang:** Software, Visualization.

Disclosure statement

No potential conflict of interest was reported by the author(s).

Funding

This research was supported in part by the China Natural Science Funds under Grant (41904033, 42204014, 42501566), the Jiangsu Province Science and Technology Plan Project under Grant (BK20230660), the Jiangsu Province Graduate Practical Innovation Project under Grant (SJCX23_1718, SJCX24_1901), and The Natural Science Foundation of the Jiangsu Higher Education Institutions of China (25KJB420005).

Data availability statement

The code for this paper is available from the corresponding authors upon reasonable request. Earthquake data were obtained from the U.S. Geological Survey (USGS) website (https://earthquake.usgs.gov/). GNSS data and products were obtained from TUSAGA-Aktif (https://www.tusaga-aktif.gov.tr/Web/DepremVerileri.aspx) and the Nevada Geodetic Laboratory (NGL) (https://geodesy.unr.edu/). The reanalysis data were obtained from https://cds.climate.copernicus.eu. The geomagnetic and solar activity indices were obtained from https://omniweb.gsfc.nasa.gov/form/dx4.html, and the TEC data were obtained from https://cdaweb.gsfc.nasa.gov/.

References

Ambrosino F, Thinová L, Briestenský M, Sabbarese C. 2019. Anomalies identification of Earth's rotation rate time series (2012–2017) for possible correlation with strong earthquakes occurrence. Geodesy Geodyn. 10(6):455–459. https://doi.org/10.1016/j.geog.2019.06.002

Bhardwaj A et al. 2017. A review on remotely sensed land surface temperature anomaly as an earthquake precursor. Int J Appl Earth Obs Geoinf. 63:158–166. https://doi.org/10.1016/j.jag.2017.08.002
Breiman L. 2001. Random forests. Mach Learn. 45(1):5–32. https://doi.org/10.1023/A:1010933404324
Chen J et al. 2024. Pre-seismic anomalies and co-seismic disturbance induced by the 2024 mw 7.1 wushi earthquake: multi-GNSS observations and modeling. Geomat Nat Hazards Risk. 15(1):2422024. https://doi.org/10.1080/19475705.2024.2422024
Chen T, Guestrin C. 2016. XGBoost: a scalable tree boosting system. In: Proceedings of the 22nd ACM SIGKDD International Conference on Knowledge Discovery and Data Mining. ACM: San Francisco, CA. p 785–794. https://doi.org/10.1145/2939672.2939785
Chen P, Liu H, Ma Y, Zheng N. 2019. Accuracy and consistency of different global ionospheric maps released by IGS ionosphere associate analysis centers. Adv Space Res. 65(1):163–174. https://doi.org/10.1016/j.asr.2019.09.042
Choudhury S, Dasgupta S, Saraf AK, Panda S. 2006. Remote sensing observations of pre-earthquake thermal anomalies in Iran. Int J Remote Sens. 27(20):4381–4396. https://doi.org/10.1080/01431160600851827
D'Incecco S, Petraki E, Priniotakis G, Papoutsidakis M, Yannakopoulos P, Nikolopoulos D. 2021. CO_2 and radon emissions as precursors of seismic activity. Earth Syst Environ. 5(3):655–666. https://doi.org/10.1007/s41748-021-00229-2
Dey S, Sarkar S, Singh RP. 2004. Anomalous changes in column water vapor after gujarat earthquake. Adv Space Res. 33(3):274–278. https://doi.org/10.1016/S0273-1177(03)00475-7
Draz MU, Shah M, Jamjareegulgarn P, Shahzad R, Hasan AM, Ghamry NA. 2023. Deep machine learning based possible atmospheric and ionospheric precursors of the 2021 mw 7.1 Japan earthquake. Remote Sens. 15(7):1904. https://doi.org/10.3390/rs15071904
Feng J et al. 2023. Analysis of ionospheric TEC response to solar and geomagnetic activities at different solar activity stages. Adv Space Res. 71(5):2225–2239. https://doi.org/10.1016/j.asr.2022.10.032
Feng J, Xiao Y, Chen J, Sun S, Ke F. 2023. A method for detecting ionospheric TEC anomalies before earthquake: the case study of ms 7.8 earthquake, February 06, 2023, Türkiye. Remote Sens. 15(21):5175. https://doi.org/10.3390/rs15215175
Fujiwara H et al. 2004. Atmospheric anomalies observed during earthquake occurrences. Geophys Res Lett. 31(17):L17110. https://doi.org/10.1029/2004GL019865
Geng J et al. 2019. PRIDE PPP-AR: an open-source software for GPS PPP ambiguity resolution. GPS Solutions. 23(4):91. https://doi.org/10.1007/s10291-019-0888-1
Guo A et al. 2023. Analyzing correlations between GNSS retrieved precipitable water vapor and land surface temperature after earthquakes occurrence. Sci Total Environ. 872:162225. https://doi.org/10.1016/j.scitotenv.2023.162225
Guo A et al. 2023. Co-seismic characterization analysis in PWV and land-atmospheric observations associated with luding ms 6.8 earthquake occurrence in China on September 5, 2022. Geomat Nat Hazards Risk. 14(1):2279494. https://doi.org/10.1080/19475705.2023.2279494
Haider SF, Shah M, Alarifi NS, Abukhadra MR. 2024. The 2023 mw 6.8 Morocco earthquake induced atmospheric and ionospheric anomalies. J Atmos Solar-Terrestrial Phys. 262:106323. https://doi.org/10.1016/j.jastp.2024.106323
Hamama I, Yamamoto M-y. 2021. Infrasonic earthquake detectability investigated in Southern part of Japan, 2019. Sensors. 21(3):894. https://doi.org/10.3390/s21030894
He Q, Shen Z, Wan M, Li L. 2020. Precipitable water vapor converted from GNSS-ZTD and ERA5 datasets for the monitoring of tropical cyclones. IEEE Access. 8:87275–87290. https://doi.org/10.1109/ACCESS.2020.2991094
Hussain E, Kalaycıoğlu S, Milliner CWD, Çakir Z. 2023. Preconditioning the 2023 kahramanmaraş (Türkiye) earthquake disaster. Nat Rev Earth Environ. 4(5):287–289. https://doi.org/10.1038/s43017-023-00411-2
Jiao Z, Shan X. 2024. A Bayesian approach for forecasting the probability of large earthquakes using thermal anomalies from satellite observations. Remote Sens. 16(9):1542. https://doi.org/10.3390/rs16091542
Jiao Z, Hao Y, Shan X. 2023. A spatially self-adaptive multiparametric anomaly identification scheme based on global strong earthquakes. Remote Sens. 15(15):3803. https://doi.org/10.3390/rs15153803
Jing F, Singh RP, Shen X. 2019. Land – atmosphere – meteorological coupling associated with the 2015 gorkha (M 7.8) and dolakha (M 7.3) Nepal earthquakes. Geomat Nat Hazards Risk. 10(1):1267–1284. https://doi.org/10.1080/19475705.2019.1573629
Jing F, Shen XH, Kang CL, Xiong P. 2013. Variations of multi-parameter observations in atmosphere related to earthquake. Nat Hazards Earth Syst Sci. 13(1):27–33. https://doi.org/10.5194/nhess-13-27-2013
Jing F, Zhang L, Singh RP, Chauhan A, Jiang M. 2024. Quasi-coseismic variations and geosphere coupling associated with the strong 2023 Turkey earthquakes. Sci Total Environ. 907:167963. https://doi.org/10.1016/j.scitotenv.2023.167963
Kalaycı İ, Özkurt Çokgüngör H. 2023. Major regional earthquakes on February 2023 in Turkey: destructive effects, economic assistances and measures on agriculture. Sci Collect «InterConf». (157):26–31.
Kane RP. 1997. Quasi-biennial and quasi-triennial oscillations in geomagnetic activity indices. Ann Geophys. 15(12):1581–1594. https://doi.org/10.1007/s00585-997-1581-1
Kato A, Ben-Zion Y. 2021. The generation of large earthquakes. Nat Rev Earth Environ. 2(1):26–39. https://doi.org/10.1038/s43017-020-00108-w
Kaufman YJ et al. 1997. Passive remote sensing of tropospheric aerosol and atmospheric correction for the aerosol effect. J Geophys Res: Atmospheres. 102(D14):16815–16830. https://doi.org/10.1029/97JD01496

Khan S, Shah M, Jamjareegulgarn P, El-Sherbeeny AM, Abukhadra MR, Khan M. 2025. Remotely sensed atmospheric anomalies of the 2022 mw 7.0 bantay, Philippines earthquake. Adv Space Res. 75(4):3692–3704. https://doi.org/10.1016/j.asr.2024.12.013

Kong X, Li N, Lin L, Xiong P, Qi J. 2018. Relationship of stress changes and anomalies in OLR data of the Wenchuan and lushan earthquakes. IEEE J Sel Top Appl Earth Observ Remote Sens. 11(8):2966–2976. https://doi.org/10.1109/JSTARS.2018.2839089

Kotzé PB. 2016. Spectral analysis of auroral geomagnetic activity during various solar cycles between 1960 and 2014. Ann Geophys. 34(12):1159–1164. https://doi.org/10.5194/angeo-34-1159-2016

Li K et al. 2025. Research on the PWV prediction model based on the ERA5-PWV calibration and WOA-RNN-BiLSTM-multihead-attention fusion algorithms. Atmos Res. 325:108238. https://doi.org/10.1016/j.atmosres.2025.108238

Li L, Li Y, He Q, Wang X. 2022. Weighted mean temperature modelling using regional radiosonde observations for the Yangtze river delta region in China. Remote Sens. 14(8):1909. https://doi.org/10.3390/rs14081909

Luhrmann F, Park J, Wong WK, Martire L, Krishnamoorthy S, Komjáthy A. 2025. Detection of ionospheric disturbances with a sparse GNSS network in simulated near-real time mw 7.8 and mw 7.5 kahramanmaraş earthquake sequence. GPS Solution. 29(1):54. https://doi.org/10.1007/s10291-024-01808-2

Ma H, Li L, Wang Y, Yu H. 2025. Abnormal changes analysis of surface temperature and water vapor before and after earthquake. Progr Geophys. 40(04):1372–1382. https://doi.org/10.6038/pg2025II0073

Maghrabi AH. 2019. Multi- decadal variations and periodicities of the precipitable water vapour (PWV) and their possible association with solar activity: Arabian Peninsula. J Atmos Solar-Terrestrial Phys. 185:22–28. https://doi.org/10.1016/j.jastp.2019.01.011

Mansouri Daneshvar MR, Tavousi T, Khosravi M. 2015. Atmospheric blocking anomalies as the synoptic precursors prior to the induced earthquakes: a new climatic conceptual model. Int J Environ Sci Technol. 12(5):1705–1718. https://doi.org/10.1007/s13762-014-0731-8

Mavroulis S, Argyropoulos I, Vassilakis E, Carydis P, Lekkas E. 2023. Earthquake environmental effects and building properties controlling damage caused by the 6 February 2023 earthquakes in east anatolia. Geosciences. 13(10):303. https://doi.org/10.3390/geosciences13100303

Nath B et al. 2024. Changes observed in land surface and air temperature after the yushu (China) (6.9 Mw) and kaikoura (New Zealand) (7.8 Mw) earthquakes using landsat thermal and geophysical datasets. J Earth Syst Sci. 133(4):231. https://doi.org/10.1007/s12040-024-02441-w

Ortega-Arroyo D et al. 2025. "Lab-Quakes": quantifying the complete energy budget of high-pressure laboratory failure. AGU Adv. 6(5):e2025AV001683. https://doi.org/10.1029/2025AV001683

Ozkula G et al. 2023. Field reconnaissance and observations from the February 6, 2023, Turkey earthquake sequence. Nat Hazards. 119(1):663–700. https://doi.org/10.1007/s11069-023-06143-2

Pulinets S, Ouzounov D. 2011. Lithosphere–Atmosphere–Ionosphere coupling (LAIC) model – an unified concept for earthquake precursors validation. J Asian Earth Sci. 41(4):371–382. https://doi.org/10.1016/j.jseaes.2010.03.005

Pulinets SA, Ouzounov D, Karelin AV, Boyarchuk KA, Pokhmelnykh LA. 2006. The physical nature of thermal anomalies observed before strong earthquakes. Phys Chem Earth, Parts A/B/C. 31(4):143–153. https://doi.org/10.1016/j.pce.2006.02.042

Rundle JB, Stein S, Donnellan A, Turcotte DL, Klein W, Saylor C. 2021. The complex dynamics of earthquake fault systems: new approaches to forecasting and nowcasting of earthquakes. Rep Prog Phys. 84(7):076801. https://doi.org/10.1088/1361-6633/abf893

Shah M, Draz MU, Saleem T. 2024. A comprehensive study on the synchronized outgoing longwave radiation and relative humidity anomalies related to global mw ≥ 6.5 earthquakes. Nat Hazards. 120(2):1421–1442. https://doi.org/10.1007/s11069-023-06262-w

Simha CP, Natarajan V, Dumka R, Rao KM. 2023. Spatial and temporal behaviour of ionospheric VTEC and atmospheric parameters before New Zealand earthquake on 13th November 2016 (M 7.8). J Appl Geophys. 212:104989. https://doi.org/10.1016/j.jappgeo.2023.104989

Tachema A. 2024. Identifying pre-seismic ionospheric disturbances using space geodesy: a case study of the 2011 lorca earthquake (Mw 5.1), Spain. EScIn. 17(3):2055–2071. https://doi.org/10.1007/s12145-024-01272-z

Tachema A, Nadji A, Bezzeghoud M. 2022. Geodetic analysis for investigating possible seismo-ionospheric precursors related to the ain Témouchent earthquake of December 22, 1999, in NW Algeria. Arabian J Geosci. 15(14):1270. https://doi.org/10.1007/s12517-022-10533-4

Tronin AA. 2006. Remote sensing and earthquakes: a review. Phys Chem Earth, Parts A/B/C. 31(4):138–142. https://doi.org/10.1016/j.pce.2006.02.024

Vecchio A, Lepreti F, Laurenza M, Alberti T, Carbone V. 2017. Connection between solar activity cycles and grand minima generation. Astron Astrophys. 599:A58. https://doi.org/10.1051/0004-6361/201629758

Wang Z, Chai H, Zheng N, Ming L, Chen P. 2025. Research on filling missing GNSS precipitable water vapor time series data using the PSORF model combined with reanalysis datasets. Measure Sci Technol. 36(1):016014. https://doi.org/10.1088/1361-6501/ad8a79

Wirth EA, Sahakian VJ, Wallace LM, Melnick D. 2022. The occurrence and hazards of great subduction zone earthquakes. Nat Rev Earth Environ. 3(2):125–140. https://doi.org/10.1038/s43017-021-00245-w

Xie B, Wu L, Sun L, Xu Y, Yoshikawa A, Mao W. 2025. Mechanism of multiple anomalies prior to Japan earthquakes from 2021 to 2023: lithosphere-coversphere-atmosphere-ionosphere coupling driven by pressure-stimulated rock current. Earth Space Sci. 12(6):e2025EA004320. https://doi.org/10.1029/2025EA004320

Yang X et al. 2023. Analytical study of the changes in brightness temperature based on the tectonic field associated with three earthquakes in the eastern Tibetan plateau. IEEE Trans Geosci Remote Sens. 61:1–15. https://doi.org/10.1109/TGRS.2023.3250554

Zhang W, Zhao J, Wang W, Ren H, Chen L, Yan G. 2013. A preliminary evaluation of surface latent heat flux as an earthquake precursor. Nat Hazards Earth Syst Sci. 13(10):2639–2647. https://doi.org/10.5194/nhess-13-2639-2013